Universidad Carlos III de Madrid

Higher Polytechnic School

Aerospace Engineering

# Aerodynamic Models for Finite Flapping Wings at Low Reynolds Numbers

Bachelor Thesis

Hasier Goitia Hernández

July 2017

uc3m

Universidad Carlos III de Madrid

Higher Polytechnic School

# Aerodynamic Models for Finite Flapping Wings at Low Reynolds Numbers

Author

Hasier Goitia Hernández

Supervisor

Alejandro Gonzalo Grande

Bachelor in Aerospace Engineering

Leganés, July 2017

**Abstract**

This thesis explores the validity of employing quasi-steady aerodynamic models to predict the forces generated by finite flapping wings at low Reynolds numbers. To this end, an actuator disk analysis (momentum theory) and a blade element method are implemented to compute the aerodynamic forces on flapping wings in two flight regimes: forward flight and hover. The actuator disk analysis is used to estimate an average value of the flow velocity induced by the wing motion. This is then considered by the blade element method along with the geometry and kinematics of the wing to compute the spanwise forces according to an available quasi-steady aerodynamic model. Since the induced velocity is dependent on the aerodynamic forces, the problem is solved in an iterative manner. Four different empirical aerodynamic models are considered: Dickinson et al. (1996), Wang et al. (2003), Dickson and Dickinson (2004), and Moriche (2017). The predictions of the models are compared to results obtained with direct numerical simulations (DNS) for the same kinematic cases. An analysis of the prediction accuracy of each model is provided as well as a proposal of some general guidelines regarding further investigation into quasi-steady aerodynamic models.

# Acknowledgments

First and foremost, I must thank Alejandro Gonzalo for devoting time and energy to this project above and beyond the call of duty. I feel fortunate to have had such a dedicated supervisor whose guidance has been both essential and personally rewarding.

I would also like to acknowledge the hard work and dedication of the professors at the Aerospace Department who have made the past four years an arduous and challenging experience, yet in the end, gratifying and fulfilling all the same.

Lastly and perhaps most importantly, I would like to sincerely thank Yves Tourigny and José Antonio Pescador for embracing the ambitious task of inspiring curiosity. They alone, more than anyone else, curved my footsteps —all those years ago— towards the path of mathematics, physics and engineering.

# Contents

# 1 Introduction

The most astounding examples of flight performance and maneuverability in the natural world are undoubtedly those found in the realm of insects. Insects were the first animal class to develop active flight and in many aspects their aerodynamic performance has remained unsurpassed by birds or indeed man-made aircraft.

The versatility of insect flight has driven the idea of creating autonomous small-scale flying robots mimicking insect flight, the so-called micro air vehicles (MAVs). Although no true MAVs exist in the present, the potential impact of MAVs on both military and civilian activities has generated great interest in the research of flapping wings for insect-like flight.

The complex flapping motion of insects allows their wings to generate substantially larger lift forces that could be achieved in steady conditions at the same speeds. Thus, the conventional aerodynamic theory which considers fixed wings moving at constant velocity has not proven useful in the study of flapping wing aerodynamics. This has led researchers to use different approaches —numerical, experimental or theoretical— to study of the unsteady mechanisms of insect flight. One of the employed methods is the direct numerical simulation (DNS), which solves the Navier-Stokes equations numerically. DNS methods provide accurate results, but have an extremely high computational cost and cannot be used to obtain immediate results. Thus, they have limited use in the design process of flapping wings.

This thesis explores the validity of simple quasi-steady aerodynamic models based on empirical data to predict aerodynamic forces of flapping wings for both forward flight and hover. A model capable of predicting aerodynamic forces accurately in near real-time would be a powerful advancement in the design of flapping wings and MAVs.

## 1.1 State of the Art

The earliest investigations into insect flight and possible aerodynamic models was carried out in the first half of the $20^{\text{th}}$ century. They were based on the application of momentum theory and quasi-steady aerodynamics. The most significant models from this period are gathered in a review by Weis-Fogh and Jensen[28]. Stolpe and Zimmer[21] observed the horizontal stroke plane of hovering insects and that the wing twist was necessary to produce lift during the up-stroke.

The effects of unsteady aerodynamics in insect flight were first discussed by Weis-Fogh[27], finding that the delayed stall and Wagner effect counteract each other. Furthermore, he observed that these effects were only important at the beginning and end of each semi-stroke, thus partly justifying the use of quasi-steady models.

Ellignton et al.[6] discussed the leading-edge vortex formation in flapping wings

and its role in the delayed stall. They found that the leading-edge vortex is a translatory effect, which can be modeled with quasi-static aerodynamics. These findings led Dickinson et al.[3] to formulate a quasi-steady aerodynamic model based on experimental data of a revolving *drosophilia melanogaster* wing at high angles of attack due to a stabilized leading-edge vortex.

An unsteady vortex lattice method (UVLM) was first implemented by Fritz and Long[8] in order to model unsteady aerodynamic effects. This was applied to flapping wings in forward flight. Ghommem et al.[9] applied a two-dimensional UVLM to avoid the noisy results caused by vorticity accumulation in three-dimensional UVLM, applying it to hovering kinematics. It was found that for high-frequency flapping wings, the 3D effects are negligible and the application of 2D unsteady aerodynamics is justified.

Ramamurti and Sandberg[17] analyzed the aerodynamics of the *drosophilia melanogaster* wing by numerically solving the incompressible Navier-Stokes equations. Sun an Tang[23] solved the complete Navier-Stokes equations by DNS on the *drosophilia virilis* wing in hover to compute the generated lift and power requirement. This study was repeated for eight different insects in Sun and Du[22].

The interested reader may find a complete review of all significant work done up to 2012 regarding aerodynamics, flight dynamics, and control of flapping-wing micro air vehicles in Taha et al.[24].

## 1.2 Objectives

Currently the most frequently used method for computing the aerodynamic forces of flapping wings is by DNS. However, these computations are very costly. The CFD group at Universidad Carlos III de Madrid has written a code to solve the incompressible aerodynamic forces of finite wings. To solve a single three-dimensional case of a pair of flapping wings, it takes approximately 250 hours on a cluster of 72 processing cores.

Evidently, the design process of flapping wings for MAVs requires a much faster solution, even at the expense of losing some accuracy in the results. Quasi-steady aerodynamic models may bridge the gap between accuracy and computational time, while also providing a sense of how each geometric and kinematic parameter affects the forces generated by the wing. The conditions under which the use of quasi-steady aerodynamics is justified is explained in section 2.1.

The objective of this thesis is to explore the available quasi-steady aerodynamic models based on empirical results and implement them for the prediction of aerodynamic forces on finite flapping wings. Each model is to be evaluated in terms of its computational cost, its prediction accuracy, and its general applicability. The ideal model is one that is applicable to any kind of flapping motion and *quickly* predicts the generated forces with *reasonable* accuracy.

The terms *quickly* and *reasonable* are used here with deliberate ambiguity. Since the design and manufacture of MAVs is still a long ways off, it is not possible at present to determine precise requirements in terms of computational cost and accuracy for plausible models.

# 2 Unsteady Aerodynamics

There are several unsteady aerodynamic phenomena that arise in flapping wings which determine the generated aerodynamic forces. There is a vast range of geometric and kinematic parameters that influence these unsteady mechanisms, which complicates the study of flapping wings. For this reason, the implementation of quasi-steady models is a powerful tool which, given its low computational cost, may be used to explore the effect of the many parameters involved in flapping wings. This section reviews the main unsteady aerodynamic mechanisms and defines the geometric and kinematic parameters that will be used in the following sections.

## 2.1 Mechanisms of Unsteady Aerodynamics

There are several unsteady aerodynamic mechanisms associated to flapping wings. Here we focus on the main three that are present in our kinematic cases (described in section 4): the delayed stall of leading edge vortices, the lift peak due to pitch-up rotation, and the wake capture due to vortical flow and airfoil interactions[20].

The delayed stall allows the wing to generate high lift coefficients at angles of attack over the stall value in steady conditions. This occurs because of the presence of a leading edge vortex, which is a flow structure that generates a low pressure area over the wing. This causes a large suction in the upper surface of the wing and produces a larger lift than would be obtained in steady conditions.

In insect-like flight, the wing experiences a fast rotation, known as a rapid pitch-up, at the end of each semi-stroke. This motion has been found to produce a peak in the aerodynamic forces –even in hover where the wing is momentarily still– due to the rotational circulation around the wing generated by the rapid pitch-up.

The wake capture occurs at the end of each semi-stroke, where fluid momentum from the vortex shed by the previous stroke is transfered to the wing. This creates a circulation around the wing, increasing the aerodynamic lift.

Given the complexity of the aerodynamic phenomena that arise in flapping wings, the range of possible geometric and kinematic parameters is incredibly vast. For this reason, there is a strong incentive to develop quasi-steady models, since they are a compromise between accuracy and computational cost.

The implementation of quasi-steady models is largely justified because the delayed stall is counteracted by the Wagner effect and the leading edge vortex is a translatory effect[24].

Taha et al.[24] propose a categorization of the type of aerodynamic models that may be applied to forward flight and hover regimes. For forward flight, quasi-steady aerodynamics are applicable for low reduced frequencies, that is, when the

velocity seen by the wing due to flapping is small compared to the flight velocity. For hover, quasi-steady aerodynamics may be applied when the flapping frequency is high since the natural frequencies of the body are much lower and cannot become coupled with the flapping frequency. In this regime, the body feels only the average forces.

## 2.2 Geometric and Kinematic Parameters

The relevant geometric and kinematic parameters used throughout this thesis are depicted in figure 1. In order to study the unsteady aerodynamics of flapping wings, we first consider a global reference system $\{x, y, z\}$, where the free-stream velocity (in forward flight) is in the direction of $\mathbf{e_x}$. The wing flaps about the origin $O$ with the wing root being at a constant distance $R$ from $O$.

The stroke plane is the plane in which the motion of the wing is contained. It is defined by the wingtip position at the end of the up-stroke, the origin $O$, and the wingtip position at the end of the down-stroke. The inclination angle of the stroke plane with respect to the $yz$ plane is $\beta$.

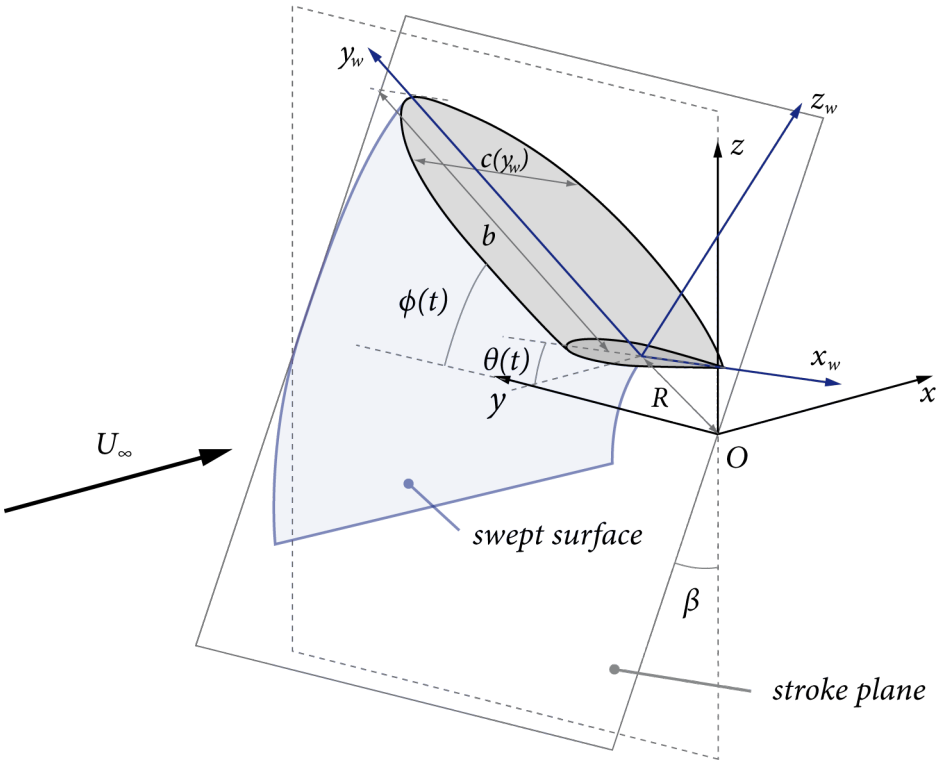


**Figure** 1: Parameters for the motion of flapping wings.

The local wing reference system $\{x_w, y_w, z_w\}$ is defined such that $y_w$ is in the direction of the wing span, $x_w$ is parallel to the chord, and $z_w$ completes the right-hand system.

The flapping angle $\phi(t)$ is the angle between $y$ and $y_w$ measured over the stroke plane. The semi-amplitude of the flapping motion is $\Phi$, such that at the end of the up-stroke $\phi(t) = \Phi$ and at the end of the down-stroke $\phi(t) = -\Phi$.

The pitch angle $\theta(t)$ is the angle between the global $x$ and the local $x_w$.

The wing itself may have any chord distribution $c(y_w)$ and a constant cross-section, which for the analyzed cases is either a NACA airfoil or an ellipse.

# 3 Methodology

To compute the forces on the flapping wing, we make use of two main tools: the blade element method and the actuator disk.

The blade element method consists on dividing the wing spanwise into several sections which are treated as two-dimensional airfoils. The kinematic parameters of each section are known functions of $y_w$ and time. The lift and drag coefficients are computed according to an aerodynamic model for each section, so that the force produced by each section is obtained. The sum of the force from each section provides the total force exerted by the wing.

However, there is one parameter that is not known. As the motion of the flapping wing causes the surrounding air to move, the flow velocity that the wing encounters is not the free-stream velocity, but rather the combination of the free-stream velocity and the velocity induced by the flapping wing. This induced velocity $\bar{\mathbf{v}}_\mathbf{i}$ must be taken into account in the blade element method. To compute it we apply the actuator disk theory, which takes an average force as input and considers conservation of momentum to estimate an average value of the induced velocity over an entire flapping period.

## 3.1 Classical Actuator Disk Theory

The *actuator disk theory*, which is also known as *momentum theory*, was developed by Rankine and Froude (1865, 1889) as a simple approximation to describe the effect of a rotor exerting a force on a fluid by generating a change in momentum. The area swept by the rotor blades is modeled as a disk of infinitesimal thickness capable of sustaining a pressure difference, acting upon the flow by accelerating it, hence the name *actuator disk*.

To illustrate this theory, let us assume a horizontal rotor in vertical flight with speed $V_\infty$ (figure 2), whose blades have a span $b$. The actuator disk is the area swept by the blades, a horizontal circle of area $S = \pi b^2$ which produces a vertical force $T$. We now consider an axially symmetric streamtube which isolates the flow passing through the disk. Taking a section of this streamtube as a control volume starting far upstream and ending far downstream of the actuator disk, we apply the conservation laws of mass, momentum and energy to find the induced velocity at the disk, $v_i$.

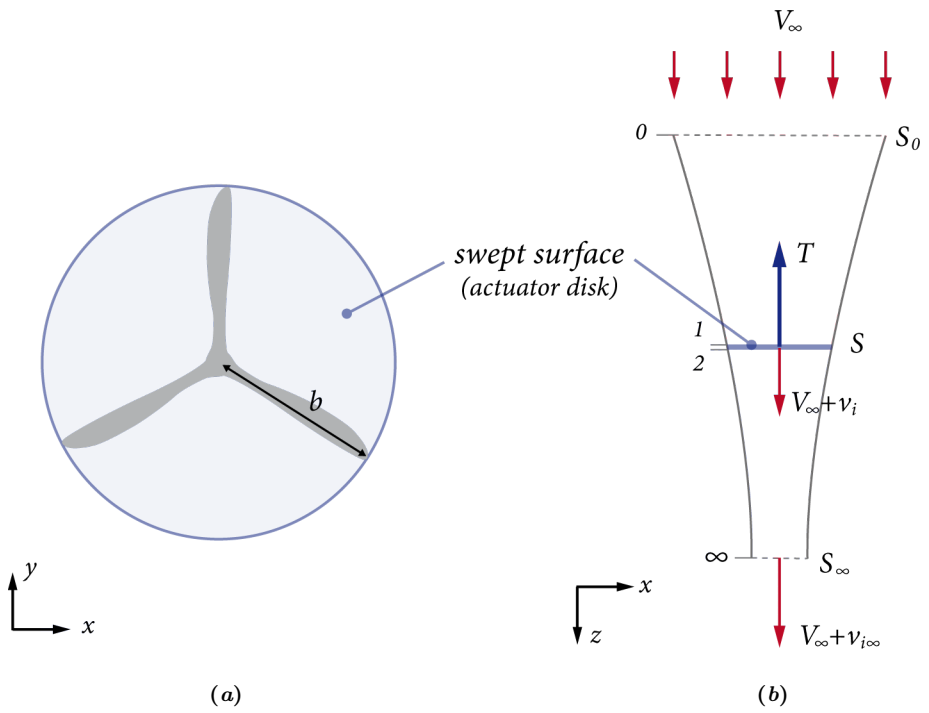


(a) (b)

**Figure** 2: (*a*) Actuator disk. (*b*) Control volume based on a streamtube of the flow generated by the actuator disk.

Since the air is considered to be incompressible, the mass flow through any cross-section of the streamtube is constant.

$$\dot{m} = \rho|\mathbf{V}_\infty|S_0 = \rho|\mathbf{V}_\infty + \mathbf{v}_i|S = \rho|\mathbf{V}_\infty + \mathbf{v}_{i\infty}|S_\infty \tag{1}$$

Conservation of momentum in the $z$ direction provides the relationship

$$-\mathbf{T} = \iint_{S_0+S_\infty} \rho\mathbf{v}(\mathbf{v}\cdot\mathbf{n})\,d\sigma = \rho\mathbf{V}_\infty|\mathbf{V}_\infty|S_0 - \rho(\mathbf{V}_\infty + \mathbf{v}_{i\infty})|\mathbf{V}_\infty + \mathbf{v}_{i\infty}|S_\infty \tag{2}$$

where $\mathbf{n}$ is the outwards-facing normal of the control volume. Combining equations 1 and 2 yields

$$\mathbf{T} = \rho S v_i \mathbf{v_{i_\infty}} \tag{3}$$

Making use of the energy equation we find the power developed by the rotor. This must be equal to the power induced to the flow, which is the product of the exerted force and the velocity at the disk.

$$P = \frac{1}{2}\dot{m}\left[(V_\infty + v_{i\infty})^2 - V_\infty^2\right] = T(V_\infty + v_i) \tag{4}$$

Recalling equations 1 and 3, equation 4 can be reduced to a simple relationship between $v_i$ and $v_{i\infty}$.

$$v_{i\infty} = 2v_i \tag{5}$$

Finally, introducing equation 5 into 3 we may express the force produced by the rotor in terms of the velocity that it induces in the flow.

$$\mathbf{T} = 2\rho S \mathbf{v}_i (V_\infty + v_i) \tag{6}$$

It is important to note that this momentum theory considers only steady flows. The magnitudes represented here are averages over a period. The thrust $T$ and the induced velocity $v_i$ are in fact the *average* thrust and *average* induced velocity generated by the rotor over a full rotation.

## 3.2 Modified Actuator Disk Theory

In order to implement the actuator disk theory to flapping wings which may be either in forward flight or hover, we perform several modifications similar to those in Morales[13]. Firstly, the area swept by a flapping wing is no longer a circle, but an annular section of amplitude $2\Phi$ (figure 3). The area of the *disk* is

$$S = \int_{-\Phi}^{\Phi} \int_{R}^{(R+b)} r dr d\theta = \Phi(2Rb + b^2) \tag{7}$$

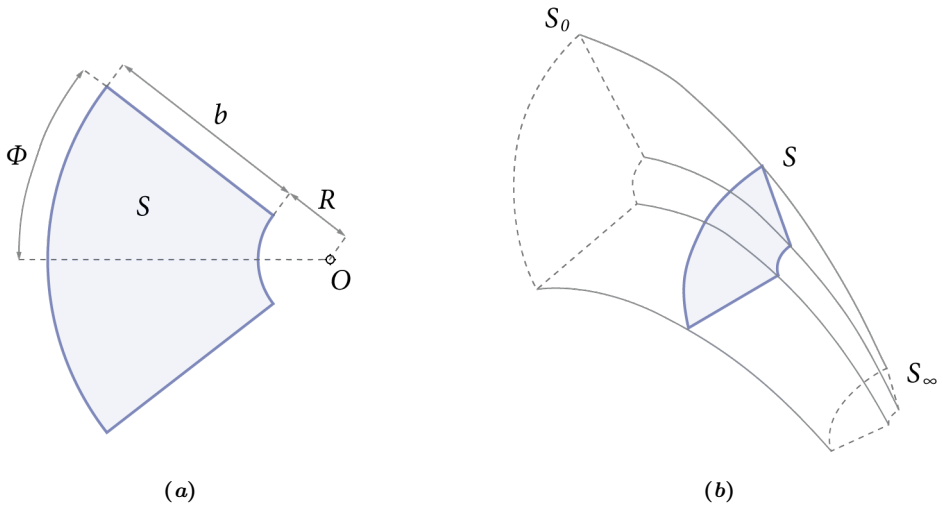


**Figure** 3: $(a)$ Geometry of the modified actuator disk. $(b)$ Example of a generic control volume obtained from a streamtube of the flow generated by the modified actuator disk.

We now consider the most general case possible for a flapping wing, illustrated in figure 4. The actuator disk is placed in a flow with a horizontal free-stream velocity $U_\infty$. The disk is oriented at an angle $\beta$ with respect to the vertical. No assumptions are made regarding the direction of the force, considering an arbitrary $\bar{\mathbf{F}} = \bar{F}_x\mathbf{e}_x + \bar{F}_z\mathbf{e}_z$[1]. In most cases, the force is —as is customary to assume in rotary wing aerodynamics— approximately perpendicular to the actuator disk, but this assumption is not necessary. The induced velocity at the disk $\bar{\mathbf{v}}_i = \bar{u}_i\mathbf{e}_x + \bar{w}_i\mathbf{e}_z$ must be parallel to the force and in the opposite direction.

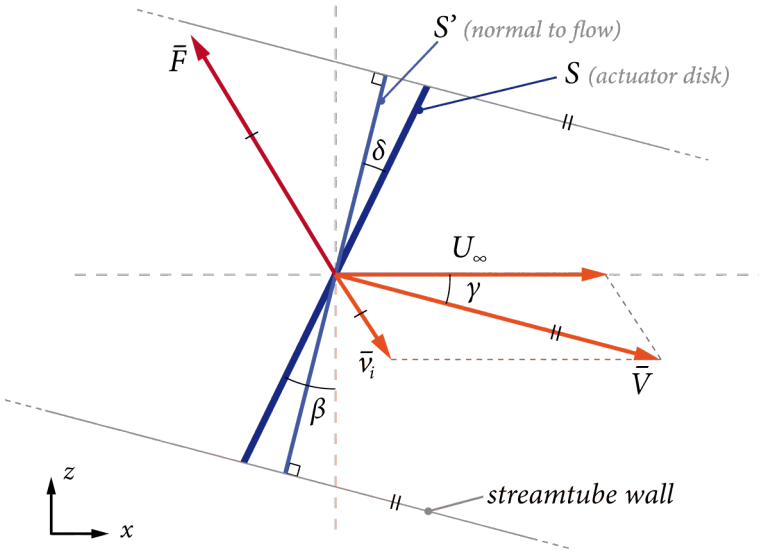


**Figure** 4: Modified actuator disk.

The total velocity at the disk is $\bar{\mathbf{V}} = (U_\infty + \bar{u}_i)\mathbf{e}_x + \bar{w}_i\mathbf{e}_z$ and forms an angle $\gamma$ with the horizontal. Since the walls of the streamtube are parallel to the velocity, the actuator disk is in fact not perpendicular to the flow (recall that $\bar{\mathbf{F}}$ is not perpendicular to the actuator disk). In order to apply the equations of conservation, we require the surface area of the cross section of the streamtube $S'$, which is the projection of the actuator disk onto the perpendicular to the flow.

$$S' = S\cos\delta \tag{8}$$

For the following application of the conservation laws, we take $S'$ as a known value. The angle $\delta$ will be discussed and introduced at the end of this analysis. The control volume is defined in the same manner as in the previous section (shown in figure 5). The conservation of mass may be applied to the control volume similarly to equation 1.

[1]Note on nomenclature: vectors are indicated by boldface (e.g. $\mathbf{a}$). The magnitude of a vector may be indicated with norm bars or written in regular font (e.g. $|\mathbf{a}| \equiv a$). Overbars are used to indicate average values (e.g. $\bar{a}$ is the average of $a$).

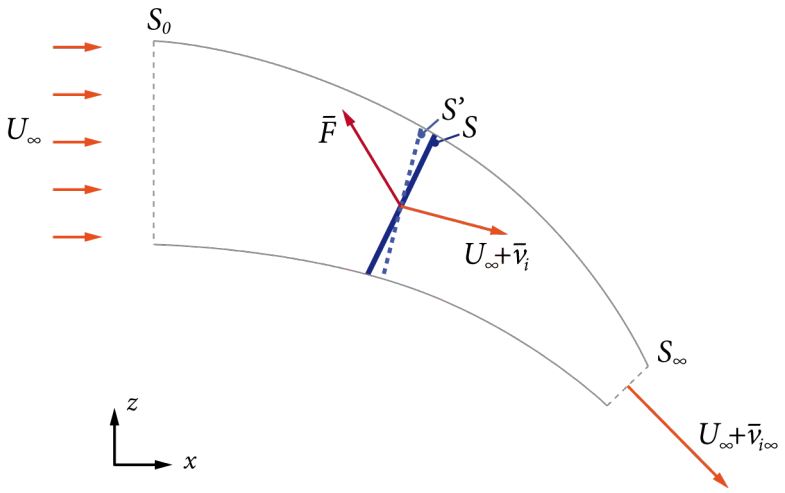


**Figure** 5: Control volume of the modified actuator disk.

$$\dot{m} = \rho|\mathbf{U}_\infty|S_0 = \rho|\mathbf{U}_\infty + \bar{\mathbf{v}}_i|S' = \rho|\mathbf{U}_\infty + \bar{\mathbf{v}}_{i\infty}|S_\infty \tag{9}$$

The conservation of momentum yields the following equation:

$$\bar{\mathbf{F}} = \iint_{S_0+S_\infty} \rho\mathbf{v}(\mathbf{v}\cdot\mathbf{n})d\sigma = -\rho\mathbf{U}_\infty|\mathbf{U}_\infty|S_0 + \rho(\mathbf{U}_\infty + \bar{\mathbf{v}}_{i\infty})|\mathbf{U}_\infty + \bar{\mathbf{v}}_{i\infty}|S_\infty \tag{10}$$

Introducing equation 9 into 10 we obtain

$$\bar{\mathbf{F}} = \rho S'|\mathbf{U}_\infty + \bar{\mathbf{v}}_i|\bar{\mathbf{v}}_{i\infty} = \dot{m}\bar{\mathbf{v}}_{i\infty} \tag{11}$$

As before, we express the induced power both in terms of the change in kinetic energy and as the product of force and velocity.

$$P_i = \frac{1}{2}\dot{m}(|\mathbf{U}_\infty + \bar{\mathbf{v}}_{i\infty}|^2 - |\mathbf{U}_\infty|^2) = \bar{\mathbf{F}}(\mathbf{U}_\infty + \bar{\mathbf{v}}_i) \tag{12}$$

Recalling the properties of vector norms, we may write $|\mathbf{U}_\infty + \bar{\mathbf{v}}_{i\infty}|^2 = |\mathbf{U}_\infty|^2 + |\mathbf{U}_\infty|^2 + 2\mathbf{U}_\infty \cdot \bar{\mathbf{v}}_{i\infty}$ and $|\bar{\mathbf{v}}_{i_\infty}|^2 = \bar{\mathbf{v}}_{i_\infty} \cdot \bar{\mathbf{v}}_{i_\infty}$. These expressions simplify equation 12 to

$$\bar{\mathbf{v}}_{i\infty} = 2\bar{\mathbf{v}}_i \tag{13}$$

Equation 11 can now be written to relate the force exerted on the flow by the actuator disk to the induced velocity at the disk.

$$\bar{\mathbf{F}} = 2\rho S' \bar{\mathbf{v}}_i |\mathbf{U}_\infty + \bar{\mathbf{v}}_i| \tag{14}$$

We now recall that $S' = S\cos\delta$. The angle $\delta$ may be expressed in terms of $\beta$ and $\gamma$. Two cases are possible depending on whether $\gamma$ is larger or smaller than $\frac{\pi}{2} + \beta$ (that is, if the total velocity points upstream or downstream of the actuator disk). Figure 6 depicts the geometrical differences of the two cases (the force has been omitted for clarity). For each case, the final equation that relates the force with the induced velocity is slightly different.

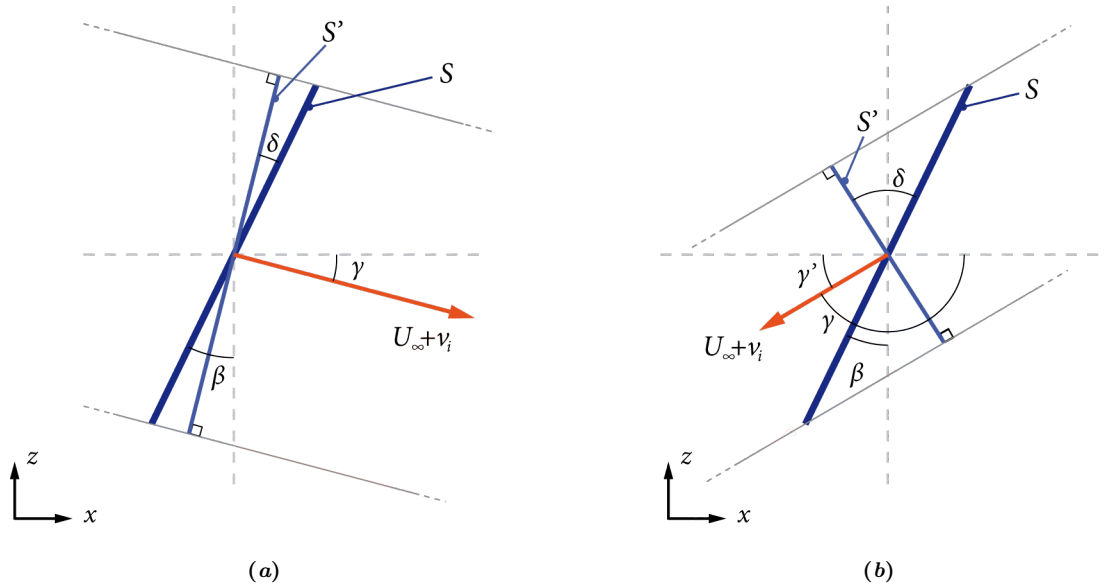


**Figure** 6: Geometry for the two possible cases: (a) $\gamma < \pi/2 + \beta$ and (b) $\gamma > \pi/2 + \beta$

**Case A:** $\gamma < \frac{\pi}{2} + \beta$

The following analysis is performed for $\bar{\mathbf{F}}$ in the first quadrant, but maintaining a coherent sign criteria, the results are valid for any direction of $\bar{\mathbf{F}}$. For this case, $\delta = \beta - \gamma$. We are interested in $\cos\delta$, which may be written as $\cos\delta = \cos\beta\cos\gamma + \sin\beta\sin\gamma$. The expressions for $\sin\gamma$ and $\cos\gamma$ are

$$\begin{aligned} \sin\gamma &= \frac{U_\infty + \bar{u}_i}{|\mathbf{U}_\infty + \mathbf{v}_i|} \\ \cos\gamma &= \frac{\bar{w}_i}{|\mathbf{U}_\infty + \mathbf{v}_i|} \end{aligned} \tag{15}$$

and therefore

$$\cos\delta = \frac{U_\infty + \bar{u}_i}{|\mathbf{U}_\infty + \bar{\mathbf{v}}_i|}\cos\beta + \frac{\bar{w}_i}{|\mathbf{U}_\infty + \bar{\mathbf{v}}_i|}\sin\beta \tag{16}$$

Substituting equations 16 and 8 into 14 and projecting the vectorial equation onto the $x$ and $y$ axes, we obtain

$$\begin{aligned} \bar{F}_x &= 2\rho S\bar{u}_i\big[\cos\beta(U_\infty + \bar{u}_i) + \sin\beta\bar{w}_i\big] \\ \bar{F}_z &= 2\rho S\bar{w}_i\big[\cos\beta(U_\infty + \bar{u}_i) + \sin\beta\bar{w}_i\big] \end{aligned} \tag{17}$$

Arranging equation 17 we obtain two equations: a quadratic equation from which $\bar{u}_i$ can be solved for and a simple relationship between $\bar{u}_i$ and $\bar{w}_i$.

$$\bar{u_i}^2\big[\cos\beta + \sin\beta\frac{\bar{F}_z}{\bar{F}_x}\big] + \bar{u}_i\big[\cos\beta U_\infty\big] - \frac{\bar{F}_x}{2\rho S} = 0 \tag{18}$$

$$\bar{w}_i = \bar{u}_i\frac{\bar{F}_z}{\bar{F}_x} \tag{19}$$

The valid solution of $\bar{u}_i$ is that which is real and in the opposite direction than $\bar{F}_x$ (recall that the signs are implicit, thus the valid solution for a positive $\bar{F}_x$ is a negative $\bar{u}_i$ and vice versa).

**Case B:** $\gamma > \frac{\pi}{2} + \beta$

For the case where the total velocity points upstream of the disk we make use of the auxiliary angle $\gamma'$ such that $\delta = \gamma' + \beta$. Given that $\gamma$ and $\gamma'$ are supplementary angles, $\sin\gamma' = \sin\gamma$ and $\cos\gamma' = -\cos\gamma$. Therefore the cosine of $\delta$ may be expressed as

$$\cos\delta = -\cos\beta\cos\gamma + \sin\beta\sin\gamma \tag{20}$$

Equation 15 still holds. Following the same procedure as in the previous case, we arrive at a quadratic equation for $\bar{u}_i$ identical to equation 18 save for a change of sign in the first-order term:

$$\bar{u_i}^2\big[\sin\beta\frac{\bar{F}_z}{\bar{F}_x} - \cos\beta\big] - \bar{u}_i\big[\cos\beta U_\infty\big] + \frac{\bar{F}_x}{2\rho S} = 0 \tag{21}$$

$$\bar{w}_i = \bar{u}_i\frac{\bar{F}_z}{\bar{F}_x} \tag{22}$$

As before, the valid solutions of $\bar{u}_i$ is that which is real and opposite in sign to $\bar{F}_x$. It is important to note that it is not possible to know *a priori* whether we are in case A or B, since only after solving for $\bar{u}_i$ can we know the direction of the total velocity.

Lastly, it should be recalled that the actuator disk theory considers only steady flow, and thus both the input force and the output induced velocity must be interpreted as average values over a flapping period. When the induced velocity is introduced in the blade element method, all points of the wing will see the same induced velocity at all points in time. This is of course not an exact representation of the real flow, but it may be valid as a first approximation.

## 3.3 Blade Element Method

The blade element theory provides a method for computing the forces exerted by a rotating wing, such as the blades of a propeller. We use this method, together with the induced velocities computed with the actuator disk theory, to predict the force exerted by the flapping wing. The blade element method consists on dividing the wing in the spanwise direction into a large number of thin sections that can essentially be treated as two-dimensional profiles. The lift and drag are computed section by section, and the total force generated by the wing is approximated as the sum of the forces on all sections.

In the limit where the wing is divided into an infinite number of sections, each of differential thickness $dy_w$, the lift and drag at each section are the spanwise lift and drag $L'(y_w)$ and $D'(y_w)$, and the sum of these forces are the integral over the span, $L = \int_0^b L'(y_w)\, dy_w$ and $D = \int_0^b D'(y_w)\, dy_w$.

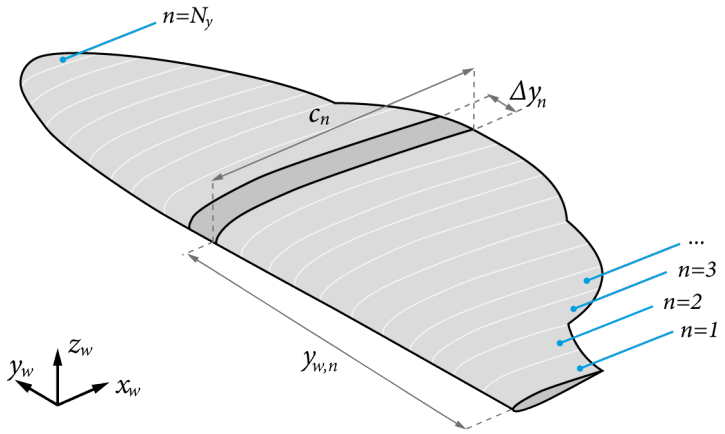


**Figure** 7: Spanwise divisions of the wing.

It is important to note that this method is not truly three-dimensional, as it does not allow for the computation of spanwise flows. Secondary 3D effects such as the velocity induced by the wing tip vortex are not accounted for. Because of this, the blade element method tends to predict slightly higher forces.

The wing is divided into $N_y$ sections (figure 7). The subindex $n$ is used to denote

the specific value of a variable dependent on $y_w$ at the $n^{th}$ section. Each section has a chord $c_n$ and width $\Delta y_n$, and its associated kinematic magnitudes are a function of both time and the spanwise coordinate. The velocity of the profile along the stroke plane is due to the flapping motion:

$$v_{\phi,n}(t) = \dot{\phi}(t)(R + y_{w,n}) \tag{23}$$

The flapping velocity is decomposed in its $x$ and $z$ components by projecting it on the stroke plane:

$$\begin{aligned} v_{\phi x,n}(t) &= v_{\phi,n}(t)\sin\beta \\ v_{\phi z,n}(t) &= v_{\phi,n}(t)\cos\beta \end{aligned} \tag{24}$$

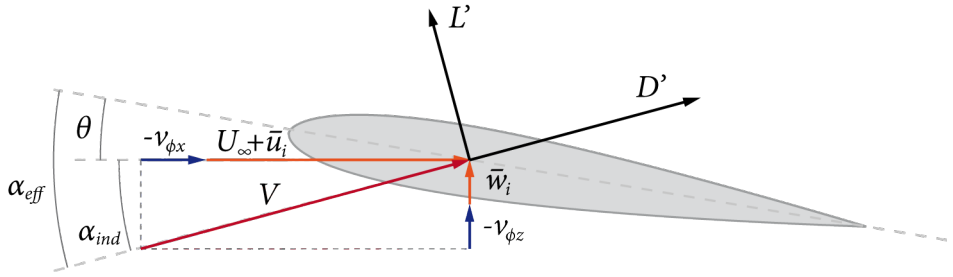


**Figure** 8: Diagram of kinematics for a two-dimensional airfoil.

The total velocity seen by the profile is obtained from the free-stream velocity, the induced velocity and the velocity due to the flapping motion (figure 8).

$$\begin{aligned} V_{x,n}(t) &= U_\infty + \bar{u}_i - v_{\phi x,n}(t) \\ V_{z,n}(t) &= \bar{w}_i - v_{\phi z,n}(t) \end{aligned} \tag{25}$$

$$V_n(t) = \sqrt{V_{x,n}(t)^2 + V_{z,n}(t)^2} \tag{26}$$

The effective angle of attack seen by each section is the sum of the pitch angle and the angle of attack induced by the velocity. The pitch angle is considered here to be constant for the entire span, since the cases being analyzed are of rigid wings with null geometric twist. However, for wings that are either flexible or present varying geometric twist, the pitch angle would also be a function of the spanwise coordinate.

$$\begin{aligned} \alpha_{ind,n}(t) &= \tan^{-1}\left(\frac{V_{z,n}(t)}{V_{x,n}(t)}\right) \\ \alpha_{eff,n}(t) &= \alpha_{ind,n}(t) + \theta(t) \end{aligned} \tag{27}$$

At this point, the spanwise force coefficients $c_l$ and $c_d$ may be computed according to one of the aerodynamic models (to be presented in section 5). For some models, $c_l$ and $c_d$ will be a function of the variables computed above, and other will require additional parameters that may be computed from these variables. In any case, the aerodynamic model will provide a spanwise lift and drag coefficient for each spanwise position and time instant.

$$\begin{aligned} c_{l,n}(t) &= f(U_\infty, v_{\phi,n}, \alpha_{eff,n}, \theta, ...) \\ c_{d,n}(t) &= f(U_\infty, v_{\phi,n}, \alpha_{eff,n}, \theta, ...) \end{aligned} \tag{28}$$

The lift and drag produced by each section at each time instant are computed:

$$\begin{aligned} L'_n(t) &= \tfrac{1}{2}\rho V_n(t)^2 c_n c_{l,n}(t) \\ D'_n(t) &= \tfrac{1}{2}\rho V_n(t)^2 c_n c_{d,n}(t) \end{aligned} \tag{29}$$

$L_n$ and $D_n$ are expressed in flow axes. In order to obtain the force in the global axes, two rotations must be made: first to the local wing axes and then to the global axes (figure 9).

$$\begin{aligned} F'_{z,n}(t) &= \left[L'_n(t)\cos\alpha_{ind,n}(t) + D'_n(t)\sin\alpha_{ind,n}(t)\right]\cos\phi(t) \\ F'_{x,n}(t) &= D'_n(t)\cos\alpha_{ind,n}(t) - L'_n(t)\sin\alpha_{ind,n}(t) \end{aligned} \tag{30}$$

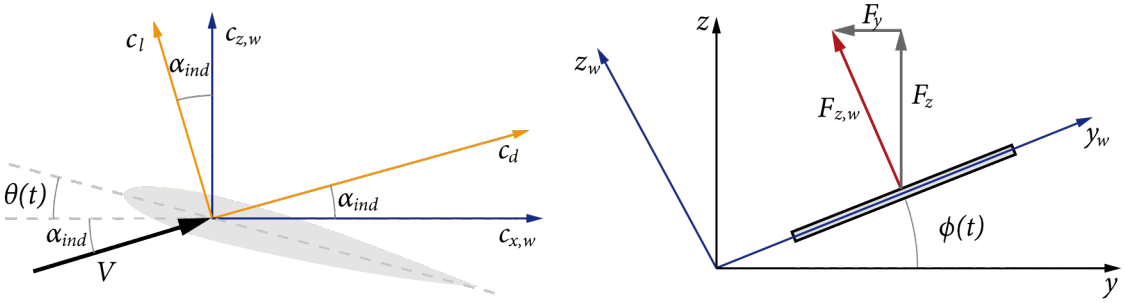


**Figure** 9: Change of axes from flow to wing and from wing to global.

The total force components in global coordinates are computed as the sum of the forces of each section (a discrete integral).

$$\begin{aligned} F_z(t) &= \Sigma_n F'_{z,n} \Delta y_{w,n} \\ F_x(t) &= \Sigma_n F'_{x,n} \Delta y_{w,n} \end{aligned} \tag{31}$$

The force coefficients are obtained normalizing the total force by the wing surface and a reference dynamic pressure constructed with the reference velocity, which is different for each kinematic case.

$$
\begin{aligned}
C_z(t) &= \frac{F_z(t)}{\frac{1}{2}\rho S_w V_{ref}^2} \\
C_x(t) &= \frac{F_x(t)}{\frac{1}{2}\rho S_w V_{ref}^2}
\end{aligned}
\tag{32}
$$

From equation 31 we must also compute the average force over a flapping period, which is required to compute the average induced velocity with the actuator disk theory. The average force is given by

$$
\begin{aligned}
\bar{F_z} &= \frac{1}{T}\int_0^T F_z(t)\,dt \\
\bar{F_x} &= \frac{1}{T}\int_0^T F_x(t)\,dt
\end{aligned}
\tag{33}
$$

## 3.4 Iterative Process

In order to compute the aerodynamic force on the wing with the blade element method, the induced velocity must firstly be computed with the actuator disk theory. However, the actuator disk requires an average force as input, which can only be computed from the output force of the blade element method. Thus, this problem must be solved by an iterative process.

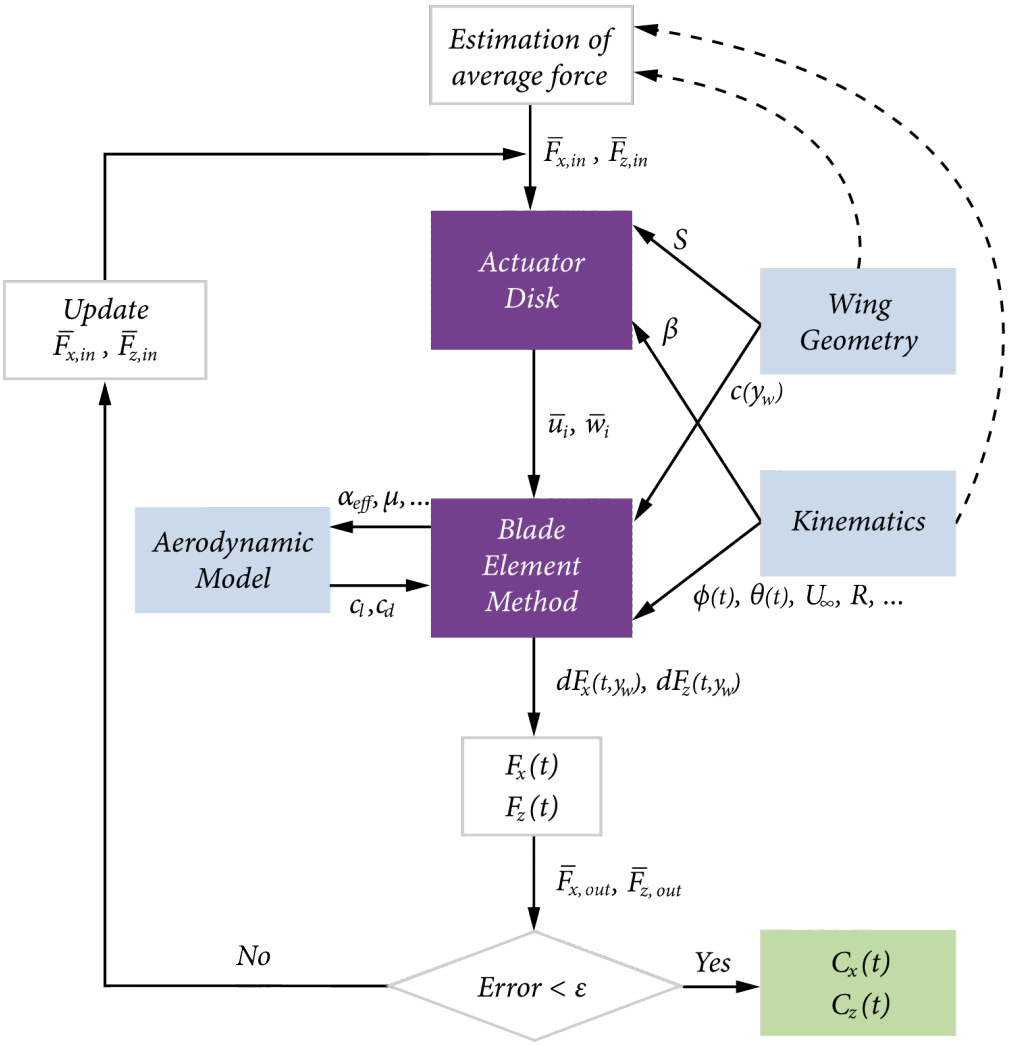


**Figure** 10: Flowchart of principal computations to be implemented. ■ Main processes, ■ inputs, □ additional computations, ■ output.

The computation is carried out as depicted in the flowchart of figure 10:

- Average forces $\bar{F}_{x,in}$ and $\bar{F}_{z,in}$ are estimated for the flapping period. These may be mere guesses or they may be estimated with a simpler model from the wing geometry and the kinematics of the problem.
- The actuator disk is used to compute the average induced velocities $\bar{u}_i$ and $\bar{w}_i$. For this, the disk area and stroke plane orientation must be computed from the wing geometry and kinematics, respectively.
- The blade element method considers the induced velocity and kinematic data to compute any parameters that the chosen aerodynamic model requires. The aerodynamic model computes the 2D lift and drag coefficients $c_l$ and $c_d$ for each section and time instant. This is used by the blade element method to compute the spanwise forces in global axes $F'_x(y,t)$ and $F'_z(y,t)$.

- The total forces $F_x(t)$ and $F_z(t)$ are computed. From these, the average forces over a whole period are computed ($\bar{F}_{x,out}$ and $\bar{F}_{z,out}$).
- The average forces obtained with the output of the blade element method ($\bar{F}_{x,out}$ and $\bar{F}_{z,out}$) are compared to those that were used in the actuator disk ($\bar{F}_{x,in}$ and $\bar{F}_{z,in}$). If the relative error is above a certain tolerance $\varepsilon$, the forces are updated (details below) and reintroduced in the actuator disk to restart the process.
- When the average forces introduced in the actuator disk and those obtained from the blade element method are within the tolerance $\varepsilon$, the forces $F_x(t)$ and $F_z(t)$ are considered accurate enough and the iterative loop is exited. The force coefficients $C_x(t)$ and $C_z(t)$ are computed and compared to the DNS results.

The error associated to the average forces is considered to be the maximum of the relative errors associated to $\bar{F}_{x,out}$ and $\bar{F}_{z,out}$. It was found that error tolerances of $\varepsilon = 1\%$ provide an adequate compromise between accuracy and computational time.

$$Error = \max\left(\left|\frac{\bar{F}_{x,out} - \bar{F}_{x,in}}{\bar{F}_{x,in}}\right|, \left|\frac{\bar{F}_{z,out} - \bar{F}_{z,in}}{\bar{F}_{z,in}}\right|\right) \tag{34}$$

Regarding the update process of $\bar{F}_{x,in}$ and $\bar{F}_{z,in}$, it was found that simply replacing the input average forces by the output average forces leads to divergent behavior. Thus, a damping factor $f_d$ was introduced. The upper limit of the damping factor is approximately $f_d = 0.45$.

$$\begin{aligned} \bar{F}'_{x,in} &= \bar{F}_{x,in} + f_d(\bar{F}_{x,out} - \bar{F}_{x,in}) \\ \bar{F}'_{z,in} &= \bar{F}_{z,in} + f_d(\bar{F}_{z,out} - \bar{F}_{z,in}) \end{aligned} \tag{35}$$

## 3.5 Error Quantification

In order to quantify the prediction accuracy of the models, some metrics are required. It is important to note, however, that the assessment of the models' accuracy is not entirely objective, since there is no single measurable criteria that expresses how well a model predicts aerodynamic forces.

We decide to base our assessment on two criteria: the mean value of the force and its amplitude. The mean value of the force is evidently a meaningful measurement of the force over time. However, several of the cases being analyzed lead to symmetric functions with a mean value approaching zero. In such cases it is necessary to observe the amplitude of the force as well to measure the accuracy of the model.

The phase delay was also considered as a possible criteria to base this assessment on. However, this results in very similar errors for all models that do not provide an adequate indication of a model's overall prediction ability. Ultimately, it was considered that using the amplitude as a criteria produced errors that better captured the performance of each model, and thus the phase delay was disregarded for this analysis.

The two errors are defined in equations 36 and 37.

$$\begin{aligned} E_{x,amp} &= \frac{C_{x,model_{max}} - C_{x,DNS_{max}}}{|C_{x,DNS_{max}}|} \\ E_{z,amp} &= \frac{C_{z,model_{max}} - C_{z,DNS_{max}}}{|C_{z,DNS_{max}}|} \end{aligned} \tag{36}$$

$$\begin{aligned} E_{x,mean} &= \bar{C}_{x,model} - \bar{C}_{x,DNS} \\ E_{z,mean} &= \bar{C}_{z,model} - \bar{C}_{z,DNS} \end{aligned} \tag{37}$$

The values $C_{x,model_{max}}$ and $C_{x,DNS_{max}}$ are the maximum force coefficients *in the mid-stroke* (the time interval when the pitch remains constant, explained in detailed in section 4.2) of the model and DNS, respectively. This is done to avoid misrepresenting the error in the cases of hover where the wing rotation causes a sharp peak (figure 11).

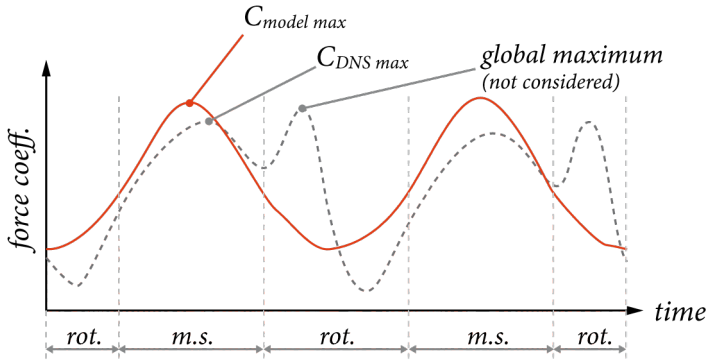


**Figure** 11: Diagram of values for amplitude error. (- - -) DNS result, (——) model result. The maximum value of the DNS result is taken only from the mid-stroke ($m.s.$) phase; the wing rotation phase ($rot.$) is disregarded.

The mean-value error is an absolute error. It is defined in this way due to the fact that in several cases the force coefficient approaches a symmetric sinusoidal function whose mean value is close to 0. Thus, defining a relative error for the mean force coefficient results in very large errors that do not provide meaningful information.

Note that the errors are not defined in absolute terms. Thus, a negative error indicates an under-prediction of amplitude or mean value, while a positive error indicates an over-prediction.

# 4 Kinematics

The aerodynamic models are implemented in two distinct flight regimes: forward flight and hover. In order to verify the models, we compare them to results obtained by DNS simulations extracted from third parties. We replicate the kinematics of the conditions in which the results were obtained so as to compare the model prediction to the DNS results.

For forward flight, the chosen simulations are those computed by the the CFD group of the Aerospace department at UC3M[10], whose database was made available for comparison. For the case of hover, the DNS results obtained by Sun and Du[22] are chosen for comparison.

## 4.1 Forward Flight

As mentioned above, the cases of forward flight are compared to simulations performed by Aerospace department at UC3M[10]. These simulations consider a wing in forward flight, flapping in a vertical stroke plane ($\beta = 0^o$) with no pitching motion ($\theta(t) = 0$). The wing is of rectangular planform ($c(y_w) = \bar{c}$) and NACA0012 airfoil section, and flaps about a point at a distance $R$ from the wing. The variable parameters of this motion are the aspect ratio of the wing (and by extension the surface area, since the mean chord is kept constant) and the distance to the pivot point $R$.

The flapping motion is a sinusoidal function such that the maximum vertical displacement at the wing tip is one mean chord. The motion begins in the middle of the up-stroke ($\phi(t_0) = 0$, $\dot{\phi}(t_0) > 0$). Thus, the flapping motion is defined as

$$\Phi = \tan^{-1}\left(\frac{\bar{c}}{R+b}\right) \tag{38}$$

$$\phi(t) = \Phi \sin(\omega t) \tag{39}$$

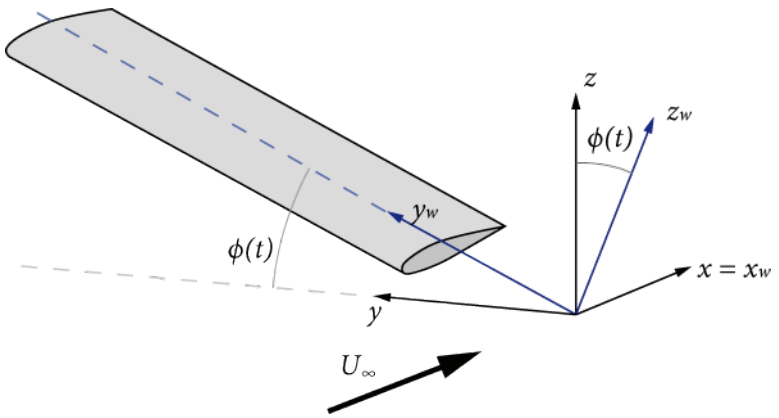


**Figure** 12: Diagram of kinematics in forward flight.

All other paremeters are kept constant. All cases are performed at reduced frequency $\kappa = \omega\bar{c}/U_\infty = 1$ and $Re = U_\infty\bar{c}/\nu = 500$, and $U_\infty$ is taken as the reference velocity.

## 4.2 Hover

The simulations by Sun and Du[22] replicate the hover flight of several insects, four of which are considered here[2]: bumblebee (*Hymenoptera, Bombus hortorum*), fruit fly (*Diptera, Drosophilia melanogaster*), hoverfly (*Diptera, Episyrphas balteatus*), and ladybug (*Coleoptera, Coccinellidae septempunctata*). For each case, the wing planform of the corresponding insect is considered (figure 13). The section is assumed to be an elliptical profile of 12% thickness.

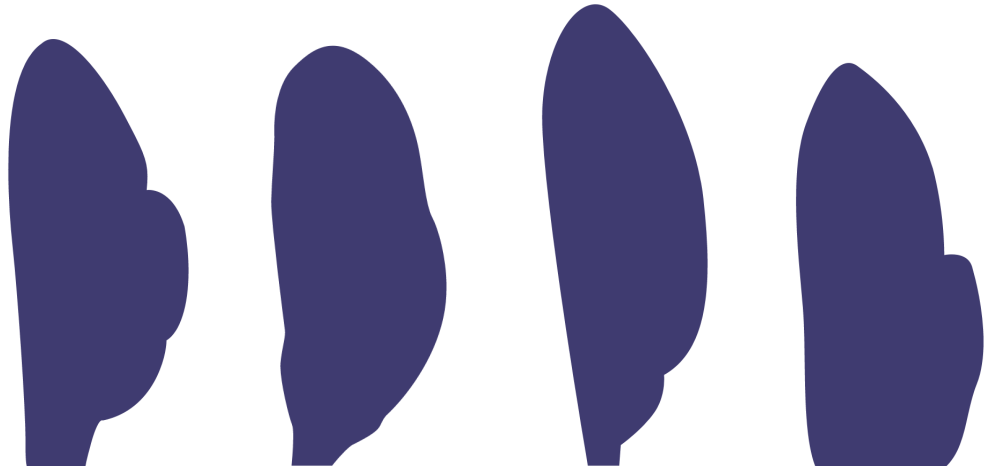

(a) Bumblebee (b) Fruit fly (c) Hoverfly (d) Ladybug

**Figure** 13: Planforms of insect wings for the cases considered in hover (extracted from Sun and Du[22], originally from Ellington[5]).

The stroke plane is horizontal ($\beta = 90^o$) and the flapping motion is considered to be a sinusoidal function which begins at the start of the downstroke ($\phi(t_0) = \Phi$, $\dot{\phi}(t_0) = 0$). In this case, the flapping semi-amplitude $\Phi$ varies for each insect (see table 1). Flapping occurs about the wing root, so $R = 0$.

$$\phi(t) = \Phi\cos(\omega t) \tag{40}$$

The pitch angle is constant except at the beginning and end of each upstroke or downstroke, where it changes from $\theta = \theta_m$ to $180^o - \theta_m$. The rotation of the wing after each semistroke lasts approxmately $\tau_r = T/4$. The midstroke pitch angle

[2]The paper by Sun and Du analyzes eight insects. However, due to a poor choice of presentation of the results, it is only possible to extract the data for four cases. For the remaining cases, it is unclear which set of data corresponds to which insect.

is also given for each insect (see table 1). The axis of the pitching rotation is considered to be located at 30% of the maximum chord from the leading edge of the wing. The motion of the wing is depicted in figure 14, and an example of the evolution of the pitch angle is shown in figure 15).

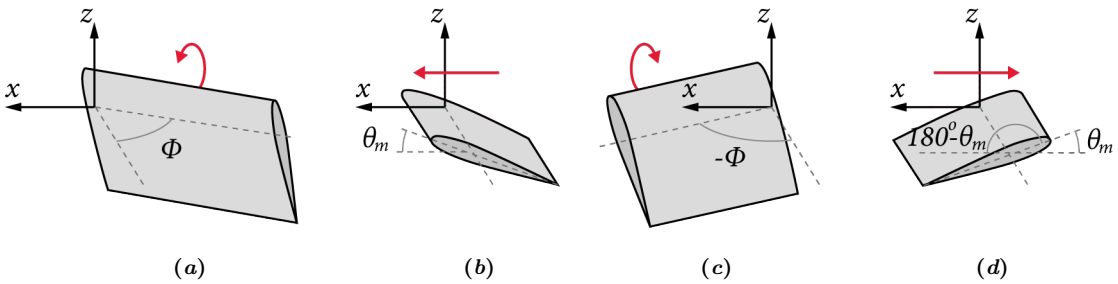


**Figure** 14: Hover kinematics, with the wing motion indicated by a red arrow. (a) The motion begins at the end of the 'upstroke' and the start of the 'downstroke', with the wing rotating to decrease the pitch angle to $\theta = \theta_m$. (b) The wing maintains a constant pitch $\theta = \theta_m$ during the middle of the 'downstroke'. (b) As the wing approaches the end of the 'downstroke' it increases its pitch angle to $\theta = 180^o - \theta_m$. (c) During the 'upstroke' the motion is symmetric to that of the 'downstroke', maintaining $\theta(t) = 180^o - \theta_m$. (d) As the wing reaches the end of the 'upstroke', it decreases the pitch angle back to $\theta = \theta_m$.

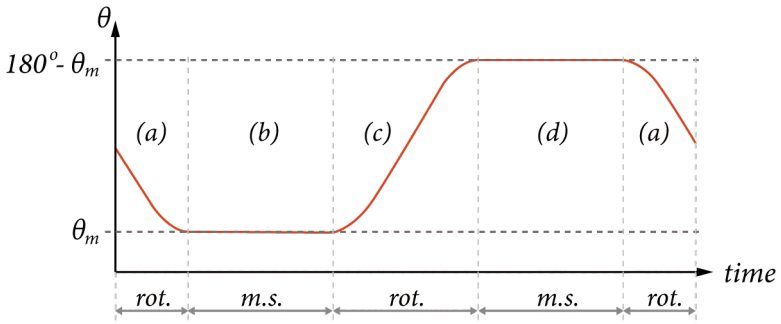


**Figure** 15: Diagram of the variation of pitch $\theta$ with time. The phases $(a)$ through $(d)$ correspond to those of figure 14. The abbreviations stand for wing rotation $(rot.)$ and mid-stroke $(m.s.)$

The relevant kinematic data for each case is gathered in table 1.

| | $\mathbf{\Phi[^o]}$ | $\mathbf{\theta_m[^o]}$ | **Re** | $\mathbf{f[s^{-1}]}$ |
|---|---|---|---|---|
| **Hoverfly** | 45 | 29 | 413 | 160 |
| **Fruit fly** | 75 | 46 | 75 | 254 |
| **Bumblee** | 58 | 28 | 1326 | 155 |
| **Ladybug** | 88 | 43 | 450 | 54 |

**Table** 1: Kinematic parameters for each insect.

The reference velocity $V_{ref}$ is arbitrarily defined as the average velocity during a semi-stroke at a distance $R_2$ from the wing root, where

$$R_2 = \sqrt{\int_0^b c(y)(y+R)^2/S_w \, dy} \tag{41}$$

The flapping velocity at $y_w = R_2$ normalized with $V_{ref}$ results in

$$\hat{v}_\phi(t, y_w = R_2) = \frac{v_\phi(t, y_w = R_2)}{V_{ref}} = \tfrac{1}{2}\pi \sin(\omega t) \tag{42}$$

# 5 Aerodynamic Models

## 5.1 Dickinson et al. (1999)

The first aerodynamic model to be considered is that developed by Dickinson et al[3]. It is based on experimental data obtained with a dynamically scaled robotic model of the fruit fly, *Drosophilia melanogaster*.

The objective of the conducted experiments was to estimate the forces generated by revolving motion alone. The experiments consisted on moving the wing through a $180^o$ arc at constant velocity and fixed angle of attack.

The results of the lift and drag coefficients were fit to sinusoidal functions of the angle of attack. No other parameters are taken into account; the proposed aerodynamic model is only a function of the effective angle of attack:

$$\begin{aligned} c_l &= 0.225 + 1.58\sin(0.037\alpha_{eff} - 0.126) \\ c_d &= 1.92 - 1.55\cos(0.036\alpha_{eff} - 0.171) \end{aligned} \tag{43}$$

## 5.2 Wang et al. (2003)

In a paper by Wang et al.[26], 2D computations of airfoils were performed and compared to the results of the previous model. The computations model an elliptic airfoil under the same kinematics as in the experiments by Dickinson et al[3], obtaining the aerodynamic forces by numerically solving the Navier-Stokes equations. The Reynolds number $Re = V_{max}c/\nu$ of these computations range from 75 to 115.

The data was also fit to sinusoidal functions of the angle of attack, obtaining the following model:

$$\begin{aligned} c_l &= 1.2\sin(2\alpha_{eff}) \\ c_d &= 1.4 - \cos(2\alpha_{eff}) \end{aligned} \tag{44}$$

This model is based axclusively on 2D aerodynamics and does not capture 3D effects of finite wings.

## 5.3 Dickson & Dickinson (2004)

The model developed by Dickson and Dickinson[4] in 2004 at the California Institute of Technology aims at predicting aerodynamic forces in forward flight. As in Dickinson et al.[3], this model is based on experimental results obtained by

a robotic model of the *Drosophilia melanogaster*. In this case the robotic model was capable of linear translational motion as the wing flaps on an inclined stroke plane, simulating forward flight.

The proposed model depends on three dimensionless paramenters: the so-called nondimensional first and second moments of inertia, $r_1$ and $r_2$, and the tip velocity ratio, $\mu$. The parameters $r_1$ and $r_2$ are based on the geometry of the wing and are defined as

$$r_1 = \frac{\int_0^b c(y)(y+R)/S_w \, dy}{R+b} \tag{45}$$

$$r_2 = \frac{\sqrt{\int_0^b c(y)(y+R)^2/S_w \, dy}}{R+b} \tag{46}$$

The tip velocity parameter is the instantaneous ratio of the chordwise component of the velocity at the wing tip due to translation and flapping. It is defined as

$$\mu(t) = \frac{U_\infty \cos\lambda(t)}{(R+b)\dot{\lambda}(t)} \tag{47}$$

The angle $\lambda$ is the projection of $\phi$ on the horizontal plane (as shown in figure 16). It may be found for a given $\beta$ and $\phi(t)$ with basic trigonometry. Applying the chain rule, we obtain its time derivative $\dot{\lambda}$.

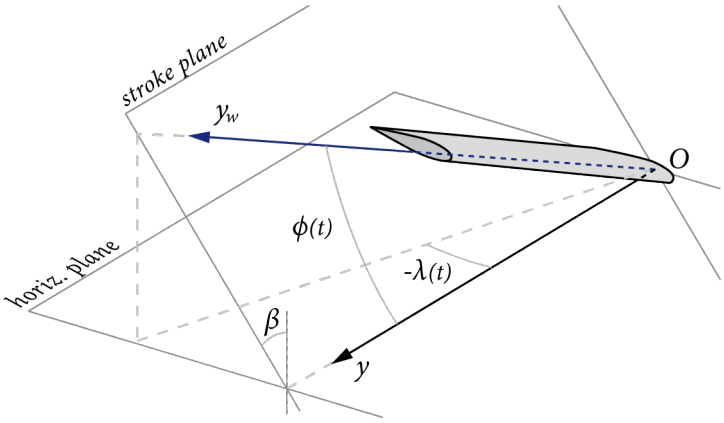


**Figure** 16: Diagram relating $\phi(t)$, $\beta$, and $\lambda(t)$. The angle $\lambda(t)$ is the projection of $\phi(t)$ on the $xy$ plane. Note that for a positive $\phi$, $\lambda$ is negative.

$$\lambda(t) = -\tan^{-1}\left[\tan\left(\phi(t)\right)\sin\beta\right] \tag{48}$$

$$\dot{\lambda}(t) = \frac{\sin\beta\dot{\phi}(t)}{\cos^2\beta\sin^2\phi(t) - 1} \tag{49}$$

Thus, the expression for the instantaneous tip velocity parameter is

$$\mu(t) = \frac{U_\infty \cos\left(-\tan^{-1}\left[\tan\left(\phi(t)\right)\sin\beta\right]\right)}{(R+b)\dot{\phi}(t)\sin\beta} \cdot \left(\cos^2\beta\sin^2\phi(t) - 1\right) \tag{50}$$

The performed experiments simulated conditions in forward flight and were used to determine empirical constants to formulate the following model:

$$\begin{aligned} c_l &= \left[\frac{1.38 + 3.30\mu + 2.01\mu^2}{r_2 + 2r_1\mu + \mu^2}\right]\sin\alpha_{eff}\cos\alpha_{eff} \\ c_d &= \left[\frac{1.38 + 2.88\mu + 1.38\mu^2}{r_2 + 2r_1\mu + \mu^2}\right]\sin^2\alpha_{eff} + \left[\frac{0.15 + 0.48\mu + 0.32\mu^2}{r_2 + 2r_1\mu + \mu^2}\right] \end{aligned} \tag{51}$$

This model considers more information that the previous ones, as it depends on the wing geometry through $r_1$ and $r_2$, on the flight mode through $\mu$, and the kinematics through $\alpha_{eff}$.

Note that the two kinematic cases being considered, forward flight with $\beta = 0^o$ and hover, impose critical values of $\mu$. For forward flight, $\mu \to \infty$ and for hover, $\mu = 0$. While these values of $\mu$ do not result in indeterminations, it is important to bear in mind that they are extreme cases for this model.

## 5.4 Moriche (2017)

The aerodynamic model proposed by Moriche[14] is based on the force decomposition by Chang[2] and the circulation model by Pesavento and Wang[15]. Its notable novelty is the prediction of the direction of the aerodynamic force, which is assumed to be perpendicular to the airfoil orientation. Thus, the force coefficients obtained by this model are not those in the flow axes ($c_l$ and $c_d$) but rather in the local wing axes ($c_{z,w}$ and $c_{x,w}$).

To facilitate the upcoming computations, let us introduce the unitary vectors $\mathbf{n_a}$ and $\mathbf{n_l}$ (figure 17). $\mathbf{n_a}$ is the vector normal to the airfoil orientation given by the pitch angle, and $\mathbf{n_l}$ is the local normal vector at a distance $l$ from the trailing edge over the airfoil surface.

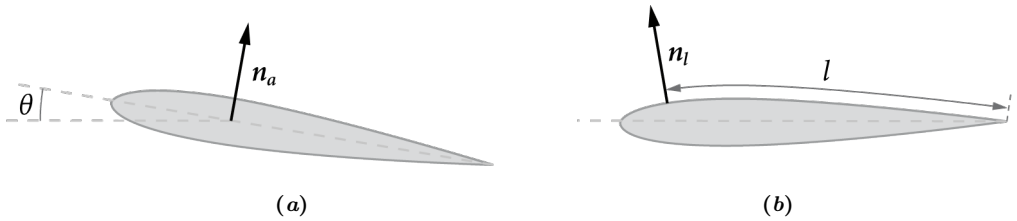


**Figure** 17: Diagram of normal vectors for Moriche's model. (a) Normal vector to airfoil $\mathbf{n_a}$. (b) Local normal vector to surface $\mathbf{n_l}$.

According to Chang's force decomposition, three separate contributions to the aerodynamic force are identified: the motion of the body ($\mathbf{F}^m$), the vorticity within the flow ($\mathbf{F}^v$) and the surface vorticity ($\mathbf{F}^s$). Thus, the vertical and Dickinson coefficients may be written as

$$\begin{aligned} c_{z,w} &= c^m_{z,w} + c^v_{z,w} + c^s_{z,w} \\ c_{x,w} &= c^m_{x,w} + c^v_{x,w} + c^s_{x,w} \end{aligned} \tag{52}$$

The term involving the surface vorticity, which includes viscous effects, is negligible with respect to the other two terms[14] and is not considered. The contribution due to the motion of the body can be modeled analytically by line integrals over the surface of the airfoil.

$$\begin{aligned} c^m_{z,w} &= \left[ -\rho \oint_l \frac{\phi_z}{V_{ref}} \frac{\partial \mathbf{v}}{\partial t} \mathbf{n_l}\, dl + \frac{\rho}{2} \oint_l |\mathbf{v}|^2 \mathbf{n_l} \cdot \mathbf{e_x}\, dl \right] \Big/ (\tfrac{1}{2}\rho V^2_{ref} l) \\ c^m_{x,w} &= \left[ -\rho \oint_l \frac{\phi_x}{V_{ref}} \frac{\partial \mathbf{v}}{\partial t} \mathbf{n_l}\, dl + \frac{\rho}{2} \oint_l |\mathbf{v}|^2 \mathbf{n_l} \cdot \mathbf{e_z}\, dl \right] \Big/ (\tfrac{1}{2}\rho V^2_{ref} l) \end{aligned} \tag{53}$$

The velocity potentials $\phi_x$ and $\phi_z$ can be computed analytically for simple geometries such as ellipses[12] but for the NACA 0012 they are computed numerically. The terms $\mathbf{v}$ and $\frac{\partial \mathbf{v}}{\partial t}$ are the velocity and acceleration of the flow at the airfoil boundary, and given the no-slip condition, they are equal to the velocity and acceleration of the airfoil. Since the kinematics are an input of the problem, $\mathbf{v}$ and $\frac{\partial \mathbf{v}}{\partial t}$ are known.

The contribution to the force due to the vorticity of the flow is given by the Kutta-Jukowski theorem, $|\mathbf{F}^v| = \rho\Gamma|\mathbf{V}|$. According to Moriche's model, this force is in the direction of $\mathbf{n_a}$. Thus, the vertical and horizontal coefficients are given by

$$\begin{aligned} c^v_{z,w} &= \frac{\rho\Gamma|\mathbf{V}|\mathbf{n_a} \cdot \mathbf{e_z}}{\frac{1}{2}\rho V^2_{ref} l} \\ c^v_{x,w} &= \frac{\rho\Gamma|\mathbf{V}|\mathbf{n_a} \cdot \mathbf{e_x}}{\frac{1}{2}\rho V^2_{ref} l} \end{aligned} \tag{54}$$

The circulation of the flow $\Gamma$ is estimated using the quasi-steady model by

Pesavento and Wang[15] for airfoils at large angles of attack and subject to large rotations.

$$\Gamma = \tfrac{1}{2} G_T c |\mathbf{V}| \sin(2\alpha_{eff}) + \tfrac{1}{2} G_R c^2 \dot{\theta} \tag{55}$$

The constants that appear in the model were fitted by Moriche to a 2D database of airfoils heaving and pitching in forward flight with $\kappa = 1.41$[14]. The values obtained were $G_T = 1.85$ and $G_R = \pi$.

Since the resulting force coefficients from this model are expressed in the local wing axes, only the axes change from local wing to global is required, so equation 30 is replaced by

$$\begin{aligned} F'_{z,n}(t) &= L'_n(t) \cos\phi(t) \\ F'_{x,n}(t) &= D'_n \end{aligned} \tag{56}$$

# 6 Results and Discussion

## 6.1 Mesh Resolution Study

A study is carried out to verify the dependence of the solution on the number of spanwise divisions. We consider the case of $N_y = 200$ as a reference well above the convergence point. A relative error based on the maximum value of the force coefficient is defined as

$$E_{max\,value}(N_y) = \frac{C_{max,N_y} - C_{max,200}}{C_{max,200}} \tag{57}$$

where $C_{max,N_y}$ is the maximum value of $C_z$ or $C_x$ for a given $N_y$ and $C_{max,200}$ is the maximum value of $C_z$ or $C_x$ for $N_y = 200$. As all models behave in a similar fashion, figure 18 presents an example of the evolution of these errors with $N_y$ for the model of Wang et al. in a case of forward flight and a case of hover. The $C_z$ in forward flight has the strongest dependence on $N_y$, though it reaches errors of less than 1% with as few as 20 spanwise divisions.

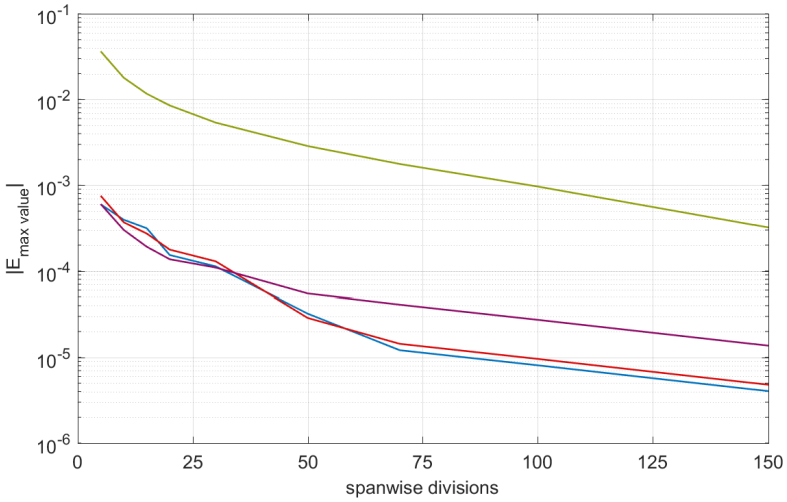


**Figure** 18: Relative max-value errors with varying $N_y$ for the Wang et al. model. (—) $C_x$ for forward flight ($AR = 2, R = 8$), (—) $C_z$ for forward flight ($AR = 2, R = 8$), (—) $C_x$ for hover (BB), (—) $C_z$ for hover (BB).

The results presented below were obtained with a resolution of $N_y = 50$. Figure 19 shows examples of the wings used for the cases of forward flight (19a) and hover (19b).

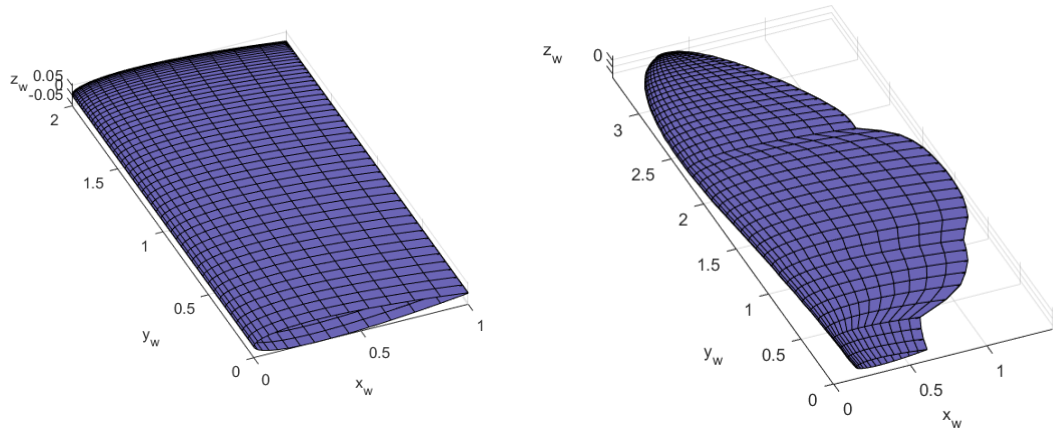


(a) Rectangular wing, $AR = 2$

(b) Bubmlebee wing

**Figure** 19: Examples of the computational domain for two wings, with 50 spanwise divisions with a sinusoidal distribution. The chordwise divisions are used only for visualization purposes and do not affect the computations.

## 6.2 Forward Flight

A selection of four cases in forward flight are presented in figures 20 through 23: $AR = 2$ with $R = 0$, $AR = 2$ with $R = \infty$, $AR = 4$ with $R = 0$, and $AR = 4$ with $R = \infty$. They are representative for all cases and illustrate the behavior of the models in forward flight. For each case, $C_z$ and $C_x$ are shown as predicted by each of the four models together with the DNS result.

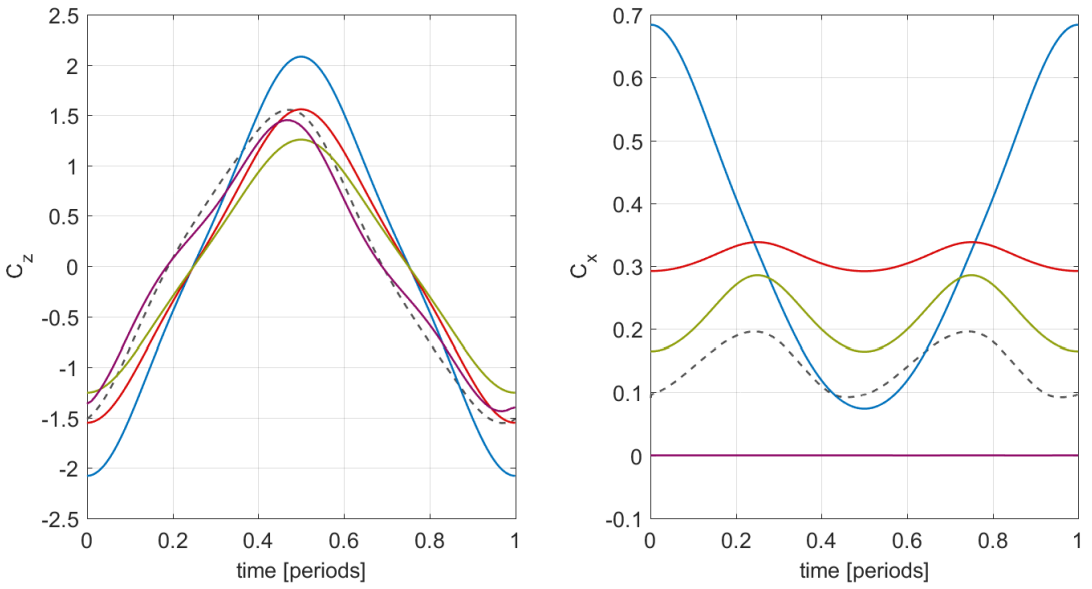


**Figure** 20: Forward flight, $AR = 2$, $R = 0$. (- - -) DNS result, (——) Dickinson et al., (——) Wang et al., (——) Dickson and Dickinson, (——) Moriche.

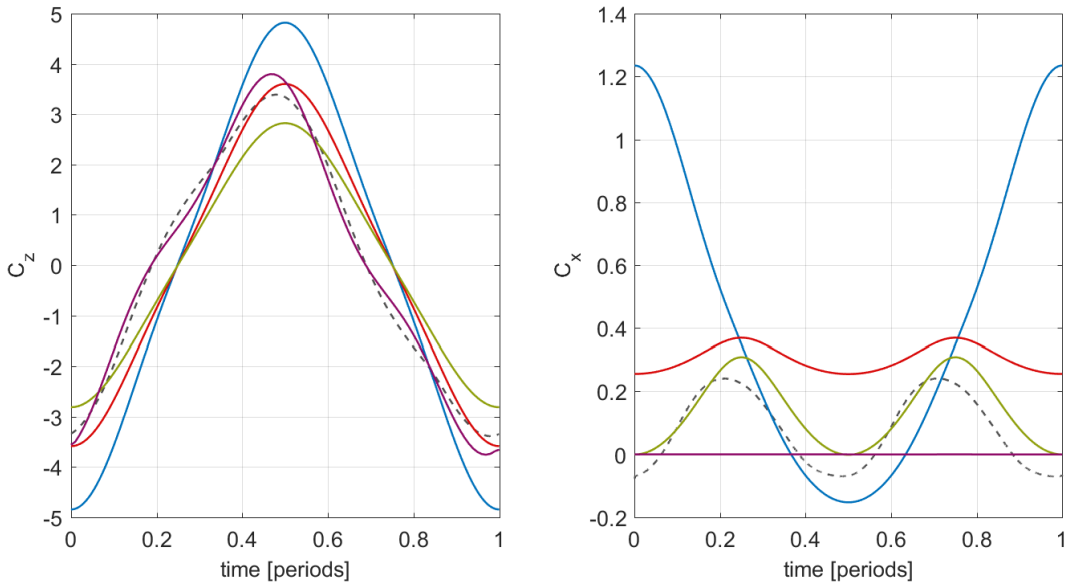


**Figure** 21: Forward flight, $AR = 2$, $R = \infty$. (- - -) DNS result, (—) Dickinson et al., (—) Wang et al., (—) Dickson and Dickinson, (—) Moriche.

In terms of the vertical force coefficient $C_z$, all four models follow the general behavior of the DNS result. The Dickinson et al. model over-predicts the amplitude of the force, while the Dickson and Dickinson model under-predicts it. The Wang et al. and Moriche models provide a better prediction of the amplitude. For all models except for Moriche's there is a phase shift with respect to the DNS, which is not constant in time (the phase shift is smallest at the mid-strokes).

Regarding the streamwise force coefficient $C_x$, the prediction of the models vary considerably. As expected, the Moriche model predicts an identically-zero streamwise force, since it assumes the force is perpendicular to the airfoil and these cases have $\theta(t) = 0$. The Dickinson et al. model predicts an incorrect behavior of $C_x$, approaching the correct values only during the down-stroke. The Wang et al. model predicts the proper shape of the force coefficient but with a larger mean value and a smaller amplitude. The Dickson and Dickinson model presents the closest approximation, despite an over-prediction of the mean value and a slight phase shift. The prediction of the Dickson and Dickinson model becomes more accurate as $R \to \infty$.

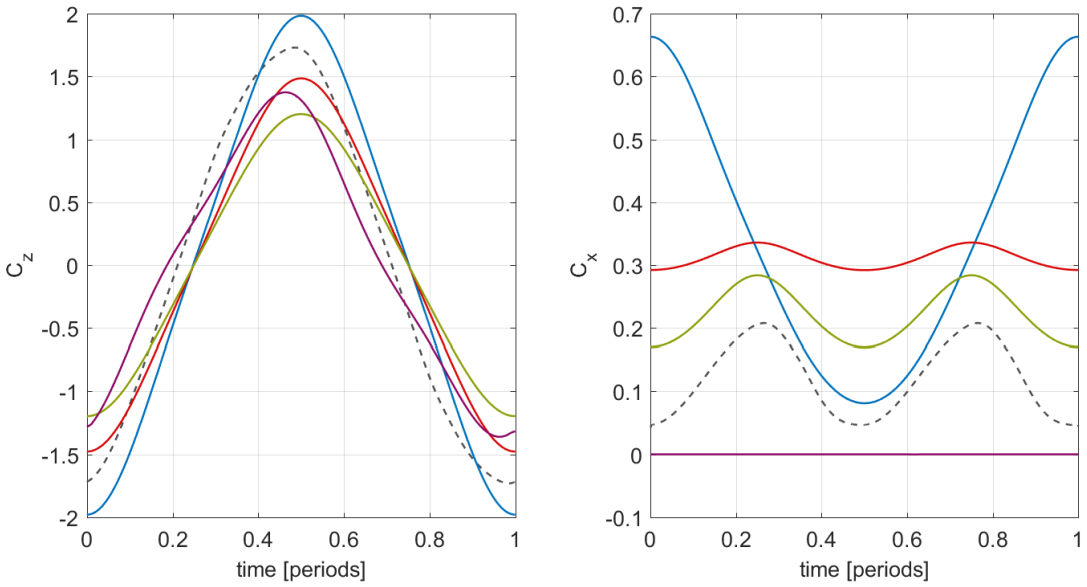


**Figure** 22: Forward flight, $AR = 4$, $R = 0$. (- - -) DNS result, (—) Dickinson et al., (—) Wang et al., (—) Dickson and Dickinson, (—) Moriche.

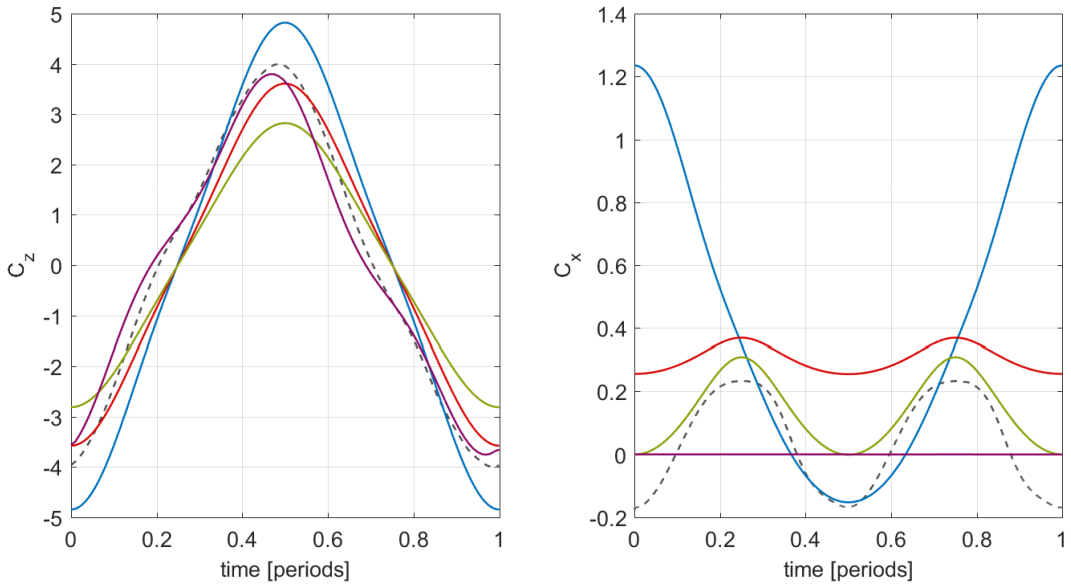


**Figure** 23: Forward flight, $AR = 4$, $R = \infty$. (- - -) DNS result, (—) Dickinson et al., (—) Wang et al., (—) Dickson and Dickinson, (—) Moriche.

The results for $AR = 2$ and $AR = 4$ are similar. Notably, the Moriche model under-predicts the vertical force for $AR = 4$ with $R = 0$ (figure 22) but regains accuracy as $R \to \infty$ (figure 23).

The errors associated to the cases of $AR = 2$ and $AR = 4$ (as defined in section 3.5) are presented in tables 2 and 3, respectively. A global average in taken for each type of error ($\bar{E}_{z,mean}$, $\bar{E}_{z,amp}$, $\bar{E}_{x,mean}$, and $\bar{E}_{x,amp}$) and each error is compared to

the global average of its type. Predictions with an error below 50% of the global error average of its type are considered 'accurate' and shown in green. Similarly, predictions with an error over 150% of the global error of its type average are considered 'poor' and shown in red.

| Case | Model | $E_{z,mean}$ | $E_{z,amp}$ | $E_{x,mean}$ | $E_{x,amp}$ |
|---|---|---|---|---|---|
| $R = 0$ | D | -0.0001 | 0.3404 | 0.2060 | 2.4895 |
| | W | -0.0045 | 0.0032 | 0.1694 | 0.7245 |
| | DD | -0.0040 | -0.1907 | 0.0776 | 0.4566 |
| | M | -0.0086 | -0.0658 | -0.1433 | -0.9998 |
| $R = 0.5$ | D | -0.0019 | 0.3658 | 0.2308 | 2.7128 |
| | W | -0.0057 | 0.0234 | 0.1845 | 0.6835 |
| | DD | -0.0050 | -0.1754 | 0.0813 | 0.4149 |
| | M | -0.0106 | -0.0519 | -0.1318 | -0.9998 |
| $R = 2$ | D | -0.0062 | 0.3754 | 0.2686 | 3.1180 |
| | W | -0.0153 | 0.0292 | 0.2002 | 0.6212 |
| | DD | -0.0068 | -0.1754 | 0.0765 | 0.3582 |
| | M | -0.0142 | -0.0217 | -0.1150 | -0.9998 |
| $R = 8$ | D | -0.0122 | 0.3954 | 0.3174 | 3.7318 |
| | W | -0.0102 | 0.0446 | 0.2160 | 0.5883 |
| | DD | -0.0089 | -0.1744 | 0.0679 | 0.3289 |
| | M | -0.0191 | 0.0474 | -0.0937 | -0.9998 |
| $R = \infty$ | D | -0.0170 | 0.4223 | 0.3550 | 4.1106 |
| | W | -0.0121 | 0.0626 | 0.2244 | 0.5276 |
| | DD | -0.0105 | -0.1675 | 0.0585 | 0.2782 |
| | M | -0.0233 | 0.1204 | -0.0800 | -0.9997 |

**Table** 2: Model errors for forward flight with $AR = 2$.

| Case | Model | $E_{z,mean}$ | $E_{z,amp}$ | $E_{x,mean}$ | $E_{x,amp}$ |
|---|---|---|---|---|---|
| $R = 0$ | D | 0.0010 | 0.1463 | 0.2232 | 2.1921 |
| | W | -0.0040 | -0.1417 | 0.1897 | 0.6160 |
| | DD | -0.0036 | -0.3058 | 0.1007 | 0.3655 |
| | M | -0.0078 | -0.2053 | -0.1221 | -0.9999 |
| $R = 2$ | D | -0.0029 | 0.1543 | 0.2720 | 2.5364 |
| | W | -0.0111 | -0.2388 | 0.2236 | 0.5243 |
| | DD | -0.0055 | -0.3036 | 0.1089 | 0.2815 |
| | M | -0.0116 | -0.1954 | -0.0974 | -0.9998 |
| $R = \infty$ | D | -0.0166 | 0.2067 | 0.3916 | 4.2897 |
| | W | -0.0235 | -0.0970 | 0.2607 | 0.5807 |
| | DD | -0.0100 | -0.2938 | 0.0949 | 0.3226 |
| | M | -0.0229 | -0.0495 | -0.0435 | -0.9997 |

**Table** 3: Model errors for forward flight with $AR = 4$.

The errors are presented graphically in figure 24, where the amplitude error is

plotted against the mean-value error for both $C_z$ and $C_x$, for all the forward flight cases. The closer a model's data points are to the origin $(0, 0)$, the closer its prediction is to the real result.

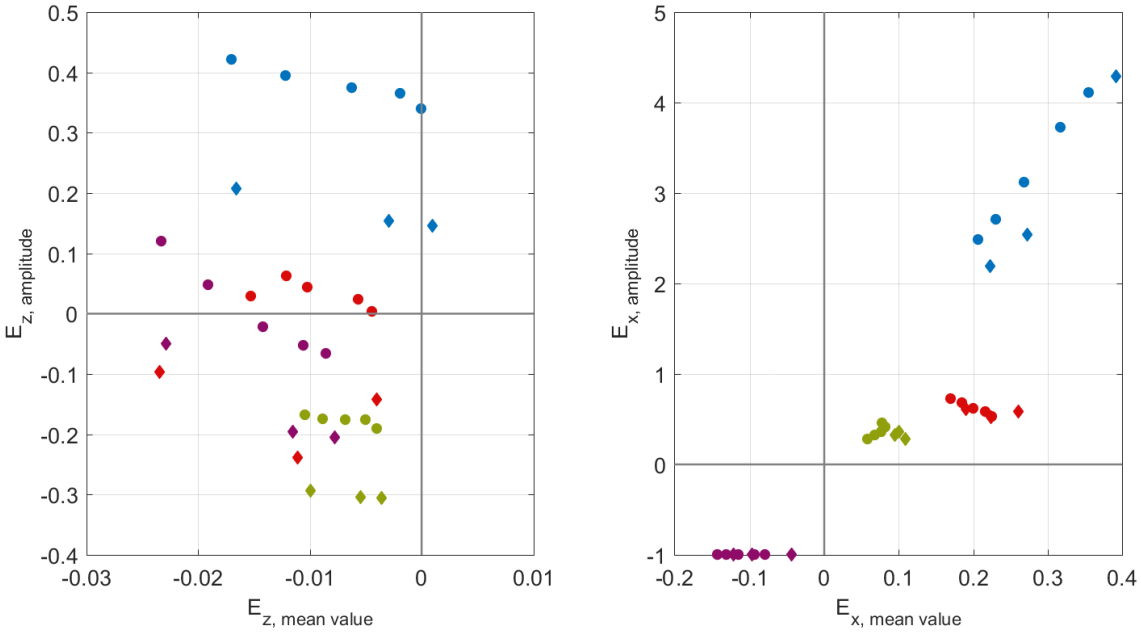


**Figure** 24: Error maps for forward flight. Models indicated by color and aspect ratio by marker shape: ■ Dickinson et al., ■ Wang et al., ■ Dickson and Dickinson, ■ Moriche; ○ $AR = 2$, ◊ $AR = 4$.

The amplitude errors of $C_z$ are consistently lower ('more negative', not necessarily closer to 0) for the cases of $AR = 4$ than for $AR = 2$. This means that for the Dickinson et al. model, which over-predicts the $C_z$ amplitude, the results are more precise for $AR = 4$ than for $AR = 2$. As the other models do not have such a strong tendency to over-predict the amplitude of $C_z$, the results for $AR = 4$ are worse that than for $AR = 2$. The $C_z$ mean value error and both $C_x$ errors seem generally unaffected by the variation in aspect ratio.

The effect of $R$ on the prediction ability does not present a general trend. The error magnitudes of $C_z$ and $C_x$ have been plotted for varying $R$ in figures 25 and 26, respectively. It is observed that the predictions of Dickinson et al. are worse for increasing $R$. For the other models, there is no general trend with $R$ observable in all errors.

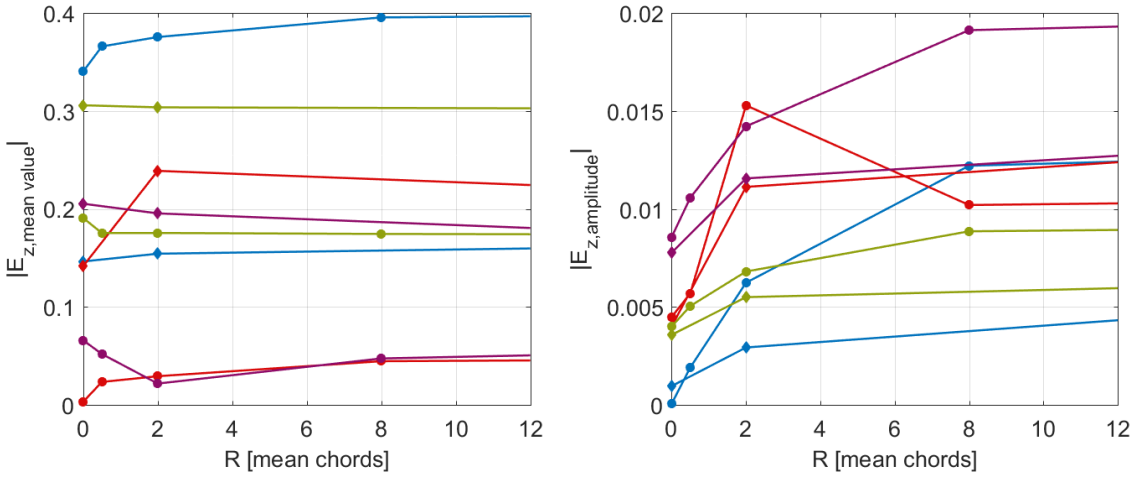


**Figure** 25: Error variation with $R$ for $C_z$. Models indicated by color and aspect ratio by marker shape: (—) Dickinson et al., (—) Wang et al., (—) Dickson and Dickinson, (—) Moriche; ○ $AR = 2$, ◊ $AR = 4$.

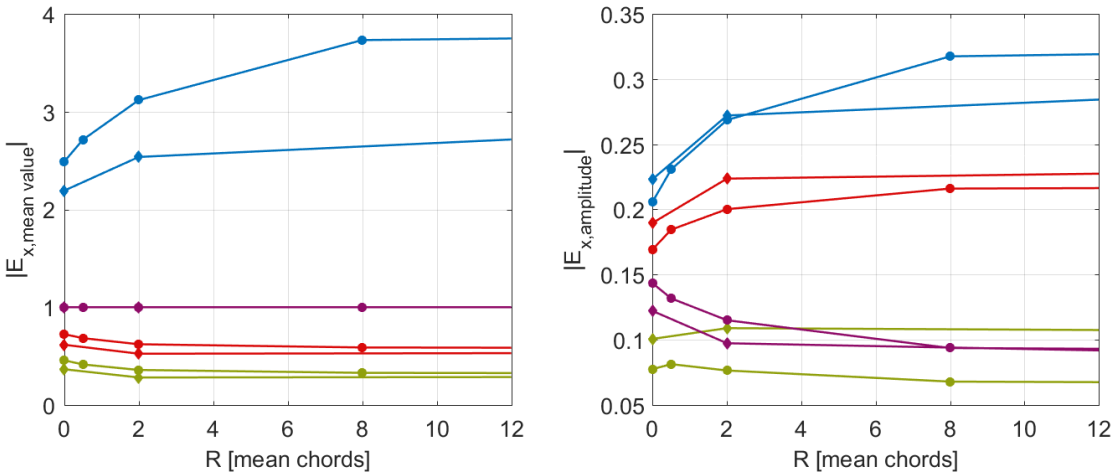


**Figure** 26: Error variation with $R$ for $C_x$. Models indicated by color and aspect ratio by marker shape: (—) Dickinson et al., (—) Wang et al., (—) Dickson and Dickinson, (—) Moriche; ○ $AR = 2$, ◊ $AR = 4$.

## 6.3 Hover

For hover, the DNS results show a sudden increase in vertical and streamwise force coefficients at the end of each semi-stroke, likely the result of rotational lift and the wake capture effect (es explained in section 2.1). This may be quite prominent as in the case of the bumblebee (figure 27) or very subtle as in the case of the fruit fly (figure 28).

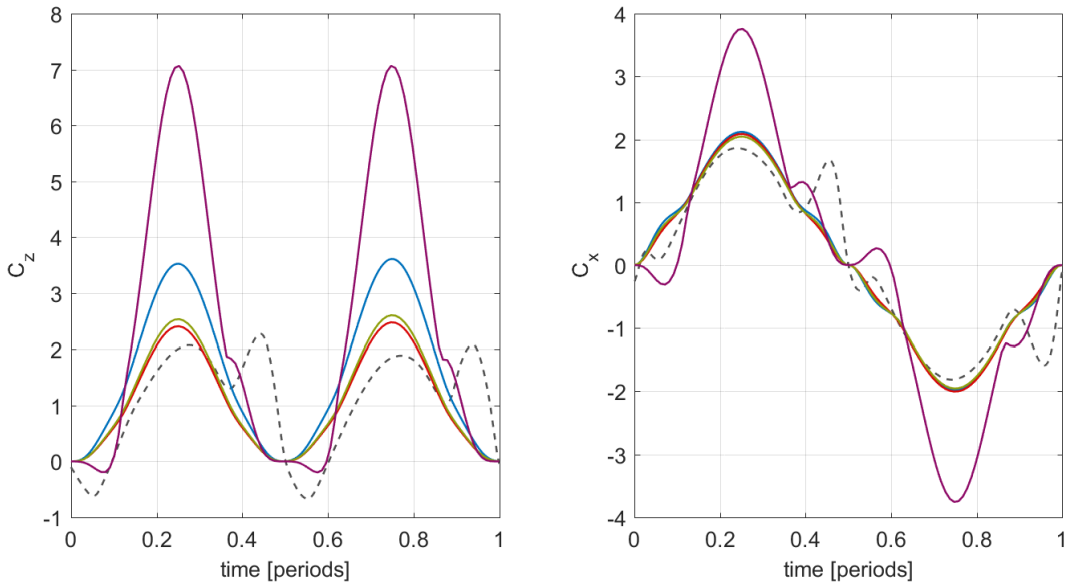


**Figure** 27: Hover, bumblebee (*Bombus hortorum*). (- - -) DNS result, (—) Dickinson et al., (—) Wang et al., (—) Dickson and Dickinson, (—) Moriche.

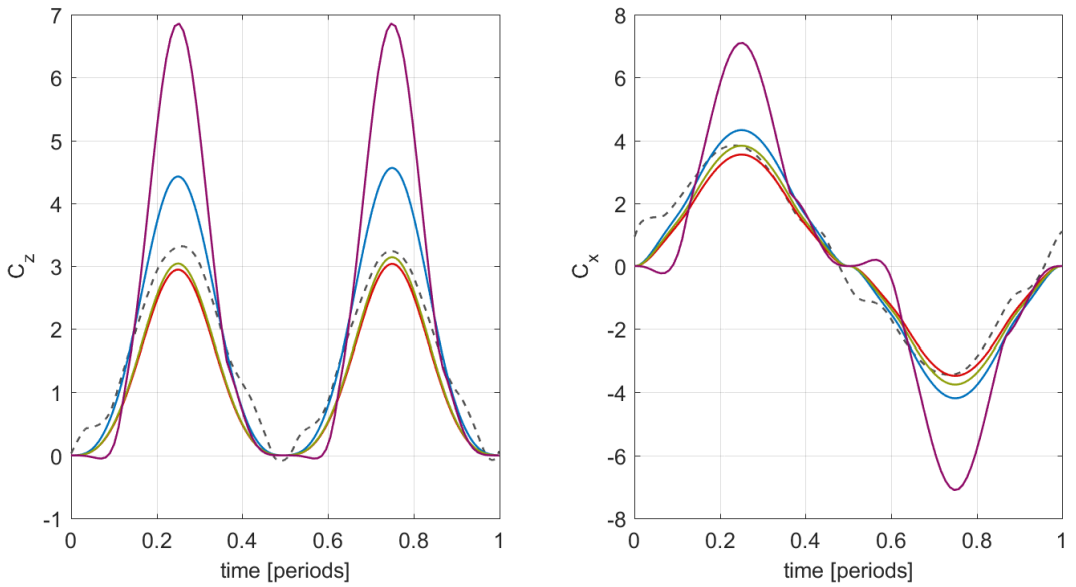


**Figure** 28: Hover, fruit fly (*Drosophilia melanogaster*). (- - -) DNS result, (—) Dickinson et al., (—) Wang et al., (—) Dickson and Dickinson, (—) Moriche.

None of the models are able to predict the increased lift at the end of each semi-stroke. However, for the cases where the force peak is prominent, the models over-predict the force in the mid-stroke section, which partly compensates for the under-prediction in the rotation phase (figure 27). In the cases where the force peak is subtle, the prediction is closer to the DNS result for the entire period (figure 28).

It is evident that Moriche's model greatly over-predicts both the vertical and streamwise forces. The other models are closer to the DNS results and all behave in a similar manner. As in the cases of forward flight, the Dickinson et al. model over-predicts the vertical force, while the Wang et al. and Dickson and Dickinson models are closer to the DNS result.

In terms of the streamwise force coefficient, all models save for Moriche's behave similarly to each other, following the low frequency of the DNS results. Interestingly Moriche's model, despite greatly over-predicting the streamwise force coefficient, presents a secondary, higher frequency that resembles the behavior of the force at the end of each semi-stroke.

As with forward flight, the errors associated to hover are presented in table 4, with 'good' predictions highlighted in green and 'poor' ones in red (the same definition as in section 6.2 is used). The error map for the hover cases is shown in figure 29.

| Case | Model | $E_{z,mean}$ | $E_{z,amp}$ | $E_{x,mean}$ | $E_{x,amp}$ |
|---|---|---|---|---|---|
| $BB$ | D | 0.4980 | 0.7006 | 0.0527 | 0.1385 |
| | W | -0.0091 | 0.1498 | 0.0309 | 0.1096 |
| | DD | 0.1632 | 0.3430 | 0.0366 | 0.2069 |
| | M | 1.3656 | 2.4097 | 0.0051 | 1.0184 |
| $FF$ | D | 0.2185 | 0.3355 | -0.1759 | 0.1280 |
| | W | -0.3800 | -0.1120 | -0.1965 | -0.0748 |
| | DD | -0.3397 | -0.0827 | -0.1953 | -0.0016 |
| | M | 0.6465 | 1.0691 | -0.2192 | 0.8517 |
| $HF$ | D | 0.2938 | 0.2649 | 0.0371 | 1.2239 |
| | W | -0.2525 | -0.1450 | 0.0118 | 1.1441 |
| | DD | -0.2288 | -0.1265 | 0.0128 | 1.0563 |
| | M | 1.0385 | 1.3925 | -0.0183 | 2.7848 |
| $LB$ | D | -0.1745 | 0.2453 | -0.1784 | 0.2841 |
| | W | -0.7140 | -0.1698 | -0.1973 | 0.0762 |
| | DD | -0.5733 | -0.0628 | -0.1927 | 0.2545 |
| | M | 0.6485 | 1.2722 | -0.2181 | 1.4523 |

**Table** 4: Model errors for hover.

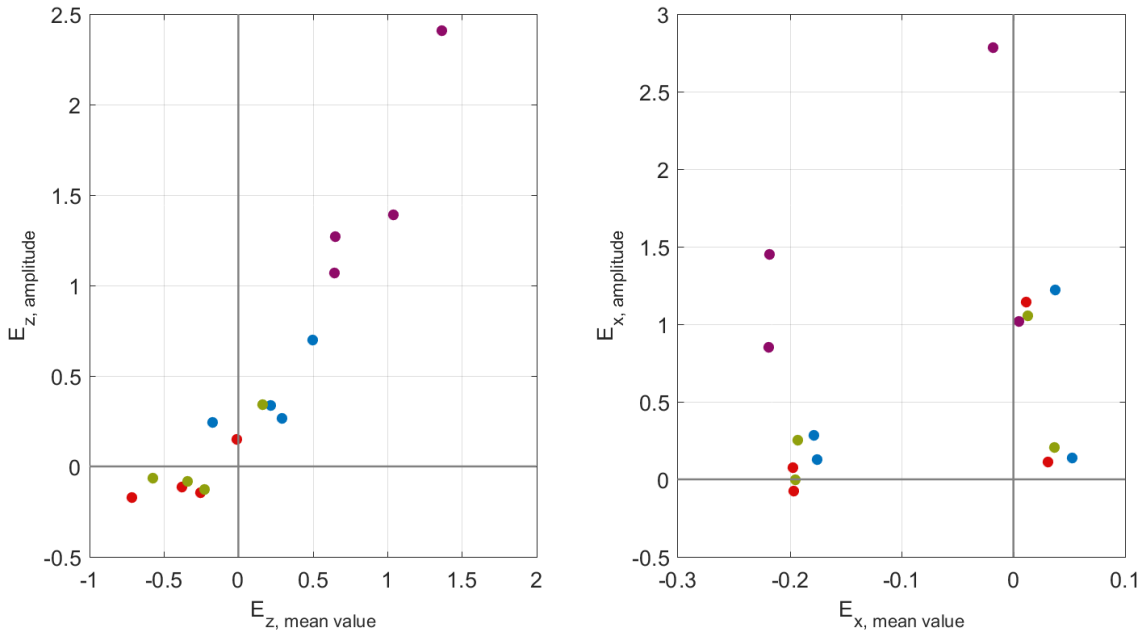


**Figure** 29: Error maps for hover. ● Dickinson et al., ● Wang et al., ● Dickson and Dickinson, ● Moriche.

As expected, the errors of the Moriche model are much larger than those of the other models. The Dickinson et al. model also consistently over-predicts the amplitude of $C_z$ in hover. For $C_x$ all models except for Moriche's present very similar errors, which vary considerably for each kinematic case.

## 6.4 Computational Cost

An approximate evaluation of the computational cost required for each model is performed. To do so, both the time taken to perform the computation and the number of cores used is taken into account. The computational cost is simply the product of both:

$$\text{Cost}_{comp.} = t_{comp.} \cdot N_{\text{cores}}$$

The computation time for each model is taken as the average time for all cases running on a desktop computer (one core). The computational cost of the DNS results is obtained using the approximate value of 250 hours running on 72 cores, $\text{Cost}_{\text{DNS}} = 9 \cdot 10^5 \cdot 72 \approx 65 \cdot 10^6 s \cdot \text{core}$ . Table 5 presents a comparison between the computational cost of the studied models and the DNS.

| Model | Cost $[s \cdot \text{cores}]$ | Fraction of DNS Cost |
|---|---|---|
| Dickinson et al. | 0.291 | $4.5 \cdot 10^{-9}$ |
| Wang et al. | 0.402 | $6.2 \cdot 10^{-9}$ |
| Dickson and Dickinson | 0.306 | $4.7 \cdot 10^{-9}$ |
| Moriche | 47.81 | $7.4 \cdot 10^{-7}$ |

**Table** 5: Computational cost of each quasi-steady model.

The Dickinson et al., Wang et al., and Dickson and Dickinson models all have computational costs lower than $0.5s \cdot \text{core}$, nine orders of magnitude less than the DNS simulations. Moriche's model has a higher computational cost than the other models by two orders of magnitude, since it requires many additional calculations, yet it is still less than a millionth of the computational cost of the DNS simulations.

## 6.5 Discussion

The following section presents the most important observations that may be extracted from the previous results regarding both the aerodynamic models and the kinematic cases.

### Dickinson et al. *vs.* Wang et al.

It is interesting to compare these two models, given that they were obtained from the same kinematics and are very similar to each other (sinusoidal functions of $\alpha_{eff}$). Recall that the Dickinson et al. model was obtained from experimental data of a finite wing while the Wang et al. model was obtained by a computational method for two-dimensional airfoils.

In the forward flight cases, the Dickinson et al. model consistently over-predicts the amplitude $C_z$ while the Wang et al. model presents a better prediction. The mean-value error for $C_z$ is close to zero for both models given the symmetry of the functions. Neither model is accurate in predicting the $C_x$, but the Dickinson et al. model is notably different from the real behavior and the data it provides is of limited practical use.

For the hover cases, the behavior of the models varies more than in forward flight. The Wang et al. model under-predicts the mean $C_z$ by different amounts while the Dickinson et al. model over-predicts the mean value of $C_z$, though more consistently. The amplitude prediction is better for Wang et al., with an error approximately half of that for Dickinson et al. In terms of the $C_x$, both models (as well as the Dickson and Dickinson model) predict essentially identical results for hover.

Based on the studied cases, the Wang et al. model is preferable to Dickinson et al. model in all regards.

The reason for the poor performance of the Dickinson et al. model in forward flight might be that it takes into account the three-dimensional aerodynamic effects. While this may seem an advantage, these effects translate poorly to a different wing with a different motion. Particularly, the coefficients of the Dickinson et al. model are highly dependent on the aspect ratio[3], as reported by Polhamus[16] and Taira[25]. On the other hand, the Wang et al. model, which is merely two-dimensional, is more versatile and can be adapted to various wings and kinematics. The comparison between these two models might point to the fact that three-dimensional effects are not overly important and that they may in fact hinder the applicability of an aerodynamic model.

### Dickson & Dickinson

In terms of the $C_z$ for forward flight, the Dickson and Dickinson model consistently under-predicts the amplitude with an error magnitude similar to that of Dickinson et al. As with the previous two models, due to the symmetrical nature of the motion it correctly predicts the mean value despite the amplitude error. Most notably, the Dickson and Dickinson model is the only one capable of predicting the $C_x$ with any reasonable accuracy, especially for large $R$.

For the cases of hover, this model behaves very similarly to the Wang et al. model, both for $C_z$ and $C_x$. Thus, considering that this model is more complex that the previous two in that it takes into account the tip velocity ratio $\mu$ and the wing geometry through $r_1$ and $r_2$, its only advantage is the prediction of $C_x$, which is clearly superior to that of any of the other models.

It is important to recall that the cases being analyzed here —forward flight with $\beta = 0^o$ and hover with $\beta = 90^o$— impose critical conditions on the tip velocity parameter, $\mu(t) = \infty$ and $\mu(t) = 0$, respectively. These cases also lose the dependency of $\mu$ with time, which might hinder the accuracy of the predicted forces. Thus, the chosen kinematic cases might not be exploiting the full potential of this model.

### Moriche

For the cases of forward flight, the Moriche model is the most precise in predicting the $C_z$, not only in terms of the amplitude and mean value, but also in the shape of the curve. The prediction of $C_x$ is, as explained previously, identically zero

[3]The paper by Dickinson et al.[3] does not explicitly state the aspect ratio of the wing used for the experiments (not any other precise geometrical parameter for that matter), but from the figures it seems that the aspect ratio of the wing is lower than 2.

because the force is assumed to be normal to the airfoil, which is horizontal for the entire motion. This results in an inaccurate prediction for these cases.

In the cases of hover, the prediction accuracy of the Moriche model is remarkably different from that in forward flight. The amplitude of the force coefficient is largely over-predicted in the mid-stroke, both for $C_z$ and $C_x$. However, this is the only model that shows the proper behavior (though far from the correct values) during the rotation of the wing at the end of each semi-stroke (figure 27). Thus, there is reason to believe that a model of this kind could, if adjusted properly, provide a force prediction more accurate than the other models.

Recall that in the Moriche model the force is decomposed in three terms, only two of which are considered: motion of the body and vorticity within the flow. The contribution of the body motion is negligible except at the wing rotation (even then, it is small compared to the contribution of the flow vorticity). Thus, the principal source of the force comes from the flow circulation, which was modeled according to Pesavento and Wang[15] as

$$\Gamma = \tfrac{1}{2} G_T c |\mathbf{V}| \sin(2\alpha_{eff}) + \tfrac{1}{2} G_R c^2 \dot{\theta}$$

The constants $G_T$ and $G_R$ determine the importance of the translation and rotation of the airfoil, respectively. Recall also that these constants were adjusted for heaving and pitching airfoils in forward flight, which explains the accuracy of the model in forward flight and its poor prediction in hover. It seems evident that the values proposed by Moriche for the flow circulation are not adequate for the kinematics of hover, being $G_T$ clearly too large and $G_R$ possibly too small.

# 7 Conclusions

This thesis has explored the capability of quasi-steady models to predict the aerodynamic forces generated by flapping-wings at low Reynolds numbers. To this end, an actuator disk analysis and a blade element method have been implemented. Four different models have been analyzed for two flight regimes: forward flight and hover. The models' predictions have been compared to DNS results for the same kinematics.

The results obtained in this thesis confirm that quasi-steady aerodynamic models can be applied to flapping wings (at least in some regimes of $\kappa$ and $f$) to obtain results of acceptable accuracy with negligible computational cost in comparison to DNS methods. However, none of the four aerodynamic models considered in this analysis have been found to be universally applicable to all cases of flapping wings.

In general terms, the main weakness of the models is the prediction of the streamwise force in forward flight. Only the Dickson and Dickinson model provides a reasonable result.

Regarding the prediction of the vertical force in forward flight, the Moriche model provides the most accurate prediction, followed by the Wang et al. model. The Dickinson et al. and the Dickson and Dickinson models provide poorer results, consistently over- and under-predicting the force, respectively. This seems to be due to the fact that these models capture 3D aerodynamic effects which are heavily dependent on the wing aspect ratio, and are thus not transferable to different wings. Given that the Wang et al. and Moriche models (both based on 2D aerodynamics) have a superior prediction ability, it seems that 2D aerodynamic models may in fact be preferable for general applicability to flapping wings. However, it is possible that in other kinematic cases the 3D effects may be more significant than in the ones studied in this thesis.

The parameter $R$ has not been found to have a global influence on the models' results. The prediction accuracy of the Dickinson et al. model decreases in all regards with increasing $R$, but for the other three models, no clear correlation between the overall accuracy and $R$ was found, as the amplitude and mean-value errors for $C_z$ and $C_x$ are affected in different manners.

In the cases of hover, the Dickinson et al., Wang et al., and Dickson and Dickinson models behave in a similar fashion, being Wang et al. slightly more accurate than the others. They predict the general behavior of the forces (both vertical and streamwise) with reasonable success but fail to capture the force peaks due to wake capture and rotational lift at the end of each semi-stroke.

The amplitude prediction of these three models decreases when the force peak at the wing rotation is large. Unfortunately, the kinematic cases studied vary several parameters in each case, and a relationship could not be established between any particular parameter and the models' accuracy.

The Moriche model provides a poor prediction in the cases of hover due to the fact that it was adjusted with a database for airfoils in forward flight. However, it is able to predict the force peaks during the wing rotation, which makes this model potentially more powerful than the others. An adjustment of the circulation parameters $G_T$ and $G_R$ is required for this model to be applicable to hover.

In terms of the computational cost, it has been verified that quasi-steady models present a great advantage over DNS. The Dickinson et al., Wang et al., and Dickson and Dickinson models have a computational cost nine orders of magnitude smaller than DNS simulations. The Moriche model, requiring more numerous and complex calculations, has a considerably larger computational cost than the other models.

In a global sense, we may conclude that from the models considered in this thesis the best option would be to use Wang et al. for the vertical force and Dickson and Dickinson for the streamwise force. This solution is generally able to predict the forces for both forward flight and hover with reasonable errors for a first approximation. Despite not being acceptable for final calculations, considering that a kinematic case may be solved in near real-time using this model, it proves to be a powerful tool in the design workflow of flapping wings.

# 8 Further Investigation

The results presented in this thesis are not entirely conclusive, as of the studied quasi-steady aerodynamic models none has been found to be universally applicable to any kinematics of flapping wing kinematics. Furthermore, the two kinematic cases studied are not sufficient to effectively evaluate the prediction ability of each model. Below are some general guidelines of the work that would be required to obtain conclusive results regarding quasi-steady models applied to flapping wings.

### Intermediate Kinematic Cases

The two kinematic cases studied in this thesis consider flapping motion in a completely horizontal ($\beta = 0^o$) or completely vertical ($\beta = 90^o$) stroke plane. This is especially detrimental to the Dickson and Dickinson model which, as explained in the results discussion, is being tested with critical values of the tip velocity parameter, $\mu(t) = \infty$ and $\mu(t) = 0$. Furthermore, knowing the behavior of the models at two extreme kinematic cases does not allow us to interpolate the results and interpret the accuracy of the models in intermediate cases of $\beta$.

Thus, it would be necessary to compare the models against DNS results of kinematic cases where $\beta$ and $\theta(t)$ are varied independently. The variation of $\beta$ would provide insight into the models' prediction ability in the transition from forward flight to hover, and allow a fair comparison between the Dickson and Dickinson model and the other models. The variation of pitching would also provide useful information in the intermediate cases between forward flight and hover, as well as better represent the behavior of the Moriche model in the prediction of $C_x$.

### Hover Database

As was mentioned in the results discussion, Moriche's circulation model was adjusted to a two-dimensional database of airfoils pitching and heaving in forward flight. This explains its good prediction ability in forward flight and its poor performance in hover. Given that the Moriche model is the only one capable of predicting the force peaks in hover due to the wing rotation at the end of each semi-stroke, it would be valuable to adjust this model for hover as well.

To this end, a database of airfoils in hover would be required. The constants $G_T$ and $G_R$ from the circulation model could be dependent on $\beta$ and $U_\infty$, providing the correct value for any kinematic case.

### Blade Element Momentum Theory

In this thesis, the actuator disk theory has been used to obtain a value of the induced velocity, which has been interpreted as an average value for the whole wing and for the entire flapping period. This simple method may be valid as a first approximation, but it may be improved to provide a better representation of the induced velocity.

The so-called *blade element momentum theory* divides the actuator disk into as many spanwise sections as the wing. Thus, a time-average induced velocity is found for each section of the wing, $\bar{\mathbf{v}}_\mathbf{i}(y_w)$. This improves the calculation of the induced velocity since the outboard wing moves faster than the inboard wing, and therefore experiences a higher induced velocity. Furthermore, the actuator disk could also be divided timewise and be treated as a quasi-steady tool, as the blade element method. The resulting induced velocity would no longer be a time-average value, but a different value for each time instant and wing section, $\mathbf{v}_\mathbf{i}(t, y_w)$.

As all models depend on the effective angle of attack, which is in turn affected by the induced velocity, a more precise estimate of the induced velocity might notably benefit the performance of the models.

Evidently, implementing these more precise methods have an inherent increase in computational cost. With the approach taken in this thesis, the iterative process is carried out once. If the same iterative process is done for every spanwise division and every time instant, the computational cost may become several orders of magnitude larger (depending on the resolution of time and geometry). Thus, it is possible that the increase in accuracy does not outweigh the additional computational cost.

# Nomenclature

### Forces and Force Coefficients

| | |
|---|---|
| $\bar{\mathbf{F}}$ | average aerodynamic force on the wing over a period |
| $\bar{F}_x, \bar{F}_z$ | horizontal and vertical components of $\bar{\mathbf{F}}$ |
| $\mathbf{F}^m$ | force due to the body motion |
| $\mathbf{F}^s$ | force due to the surface vorticity |
| $\mathbf{F}^v$ | force due to the flow vorticity |
| $c_l, c_d$ | 2D lift and drag coefficients (normal and parallel to the flow) |
| $C_z, C_x$ | vertical and horizontal force coefficients |
| $F'_z, F'_x$ | vertical and horizontal spanwise forces |
| $F_z, F_x$ | total vertical and horizontal forces |
| $L', D'$ | spanwise lift and drag forces (normal and parallel to the flow) |

### Geometric Parameters

| | |
|---|---|
| $\bar{c}$ | mean geometric chord |
| $\beta$ | tilt angle of the stroke plane with respect to the $yz$ plane |
| $\Delta y_{w,n}$ | width of the $n^{th}$ wing section |
| $\delta$ | angle formed by the stroke plane and the plane normal to the flow velocity |
| $\gamma$ | angle from $\bar{\mathbf{V}}$ to $\mathbf{e_x}$ |
| $\gamma'$ | angle from by $\bar{\mathbf{V}}$ to $-\mathbf{e_x}$ |
| $\lambda$ | projection of $\phi$ on the horizontal plane |
| $\mathbf{e_x}, \mathbf{e_z}$ | unitary vectors in the global $x$ and $z$ directions |
| $\mathbf{n_a}$ | unitary vector normal to airfoil orientation |
| $\mathbf{n_l}$ | unitary vector normal to airfoil surface at a distance $l$ from the trailing edge |
| $\mathbf{n}$ | unitary vector normal to the actuator disk |
| $b$ | wing span |
| $c(y_w)$ | chord distribution |
| $c_n$ | chord length at the $n^{th}$ wing section |
| $N_y$ | number of spanwise divisions |
| $O$ | Origin of global axes; center of flapping motion |
| $R$ | Distance from $O$ to wing root |
| $r_1$ | nondimensional first moment of inertia wing radius |
| $R_2$ | second moment of inertia wing radius |

| | |
|---|---|
| $r_2$ | nondimensional second moment of inertia wing radius |
| $S$ | surface area of the actuator disk |
| $S'$ | surface area of the projection of the actuator disk on a plane normal to the flow velocity |
| $S_0$ | surface area of the streamtube far upstream of the actuator disk |
| $S_\infty$ | surface area of the streamtube far downstream of the actuator disk |
| $S_w$ | wing surface area |
| $x, y, z$ | Global axes |
| $x_w, y_w, z_w$ | Local wing axes |

**Kinematic Parameters**

| | |
|---|---|
| $\alpha_{eff}$ | effective angle of attack |
| $\alpha_{ind}$ | induced angle of attack |
| $\bar{\mathbf{V}}$ | total velocity at the actuator disk |
| $\kappa$ | reduced frequency |
| $\bar{\mathbf{v}}_\mathbf{i}$ | induced velocity at actuator disk |
| $\bar{\mathbf{v}}_{\mathbf{i}\infty}$ | induced velocity far downstream of the actuator disk |
| $\mathbf{V_n}$ | total velocity seen by the $n^{th}$ wing section |
| $\mathbf{v}$ | flow velocity |
| $\omega$ | angular frequency |
| $\Phi$ | semi-amplitude of flapping motion |
| $\phi$ | flapping angle |
| $\tau_r$ | wing rotation period |
| $\theta$ | pitch angle |
| $\theta_m$ | pitch angle at the mid-stroke |
| $f$ | frequency of flapping motion |
| $T$ | period of flapping motion |
| $t$ | time |
| $U_\infty$ | free-stream velocity |
| $u_i, w_i$ | horizontal and vertical components of $\mathbf{v_i}$ |
| $u_{i\infty}, w_{i\infty}$ | horizontal and vertical components of $\mathbf{v_{i\infty}}$ |
| $v_{\phi,n}$ | velocity at the $n^{th}$ wing section due to flapping |
| $V_{ref}$ | reference velocity |
| $V_{x,n}, V_{z,n}$ | horizontal and vertical components of $\mathbf{V_n}$ |

**Other Symbols**

| | |
|---|---|
| $\dot{m}$ | mass flow rate |
| $\Gamma$ | circulation |
| $\mu$ | tip velocity parameter |
| $\nu$ | kinematic viscosity |
| $\phi_x, \phi_z$ | $x$ amd $z$ velocity potentials |
| $\rho$ | air density |
| $G_T, G_R$ | translational and rotational constants for circulation model |
| $P$ | power induced by the wing |
| $Re$ | Reynolds number |
| $V_\infty$ | free-stream velocity in vertical flight |

# A Socio-Economic Environment

## A.1 Project Budget

The budget associated to the development of this bachelor thesis is not particularly relevant, since no amount of money or other resources were specifically spent on this project. The code is written entirely in Matlab, which due to university agreements could be used for this purpose free of charge. Because a bachelor thesis is, by definition, part of an undergraduate's academic studies, I received no payment for my work. The only quantifiable resource spent on this project is the time dedicated by the supervising professors. At an estimated rate of 15€/h, their dedication to this project —roughly three hours per week for four months— comes at a total of 720€.

The budget would present notable differences if the project was carried out at a private company. Firstly, a standard commercial-use Matlab license has a price of 2000€[4]. Also, considering the author to be a recently graduated intern, he would optimistically earn 9€/h. The total time spent on this thesis is approximately 300h (12ETC · 25h/ETC), so the intern would be paid 2700€. The cost of having the input from an experienced engineer would remain at 720€.

| | Student/ Intern | Input from Experienced Engineer | Matlab License | **Total** |
|---|---|---|---|---|
| University Thesis | 0€ | 720€ | 0€ | **720€** |
| Company Project | 2700€ | 720€ | 2000€ | **5420€** |

**Table** 6: Project budget different environments.

## A.2 Socio-Economic Impact

The findings of this thesis are a positive contribution in the study of quasi-steady aerodynamic models that may be used in the design workflow of MAVs and perhaps even in the MAV processor for real-time flight computations. While this thesis alone will not have any significant socio-economic impact, the eventual design of MAVs will undoubtedly change many military, civilian, and scientific activities.

The military sector has expressed great interest in the development of MAVs given their versatility as portable reconnaissance devices. They could be used for scouting enemy positions, provide live tactical combat information or take aerial images of the surrounding area, all with no threat to human lives.

[4] As of July 2017. At this price, the option of implementing the code in a different programming language such as Fortran or Python might be considered.

In terms of civil applications, similar activities could be used by the police force and the firefighting departments. In either a hostage situation or a building fire, MAVs would be useful in providing visual information of a dangerous area with no risk to human lives. Scientists at the Georgia Institute of Technology have also shown interest in using MAVs to support rovers in the Mars exploration, since given the planet's thin atmosphere fixed-wing flight is not viable.

This thesis is a small contribution to the aerodynamic study of flapping wings, of which many top-level researchers worldwide are part of and whose work will, in the near future, have an important impact on our society.

# B Regulatory Framework

In the past years, unmanned aircraft have experienced a significant increase in popularity, mostly due to recreational use of lightweight consumer electronic drones. Most countries have issued legislation regarding the use of drones which would be applicable to MAVs. However, the legal framework around drones is still changing as new models emerge and usage trends develop. In Europe the regulation is quite fragmented with legislation varying from country to country.

In Spain, the main regulation regarding the use of drones can be found in the Real Decreto-ley 8/2014, although several modifications have been made to date and additional changes in regulation in the near future are expected. EASA is currently attempting to homogenize the legal framework regarding drones in the European Union, having recently published a notice of proposed amendment (NPA)[7] to address this issue. Given the rapidly-changing nature of regulation, it is difficult to predict the legal framweork MAVs would be subject to in the future.

In any case, this thesis is merely a research project far from the actual implementation of MAVs. The only regulation that could apply would be that regarding intellectual property. However, the information acquired from other publications used in this thesis may be freely used by anyone who purchases the rights to the publications —as the University does— so there is no issue in that regard. Thus, there is no regulatory framework that directly affects this thesis.

# C Results for Forward Flight

## AR = 2

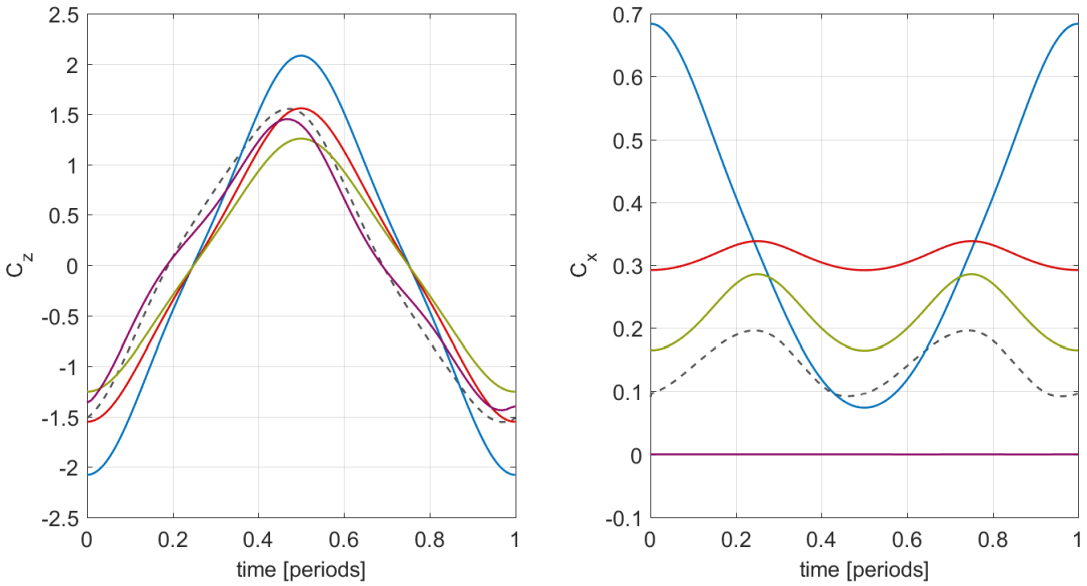


**Figure** 30: Forward flight, $AR = 2$, $R = 0$. (- - -) DNS result, (—) Dickinson et al., (—) Wang et al., (—) Dickson and Dickinson, (—) Moriche.

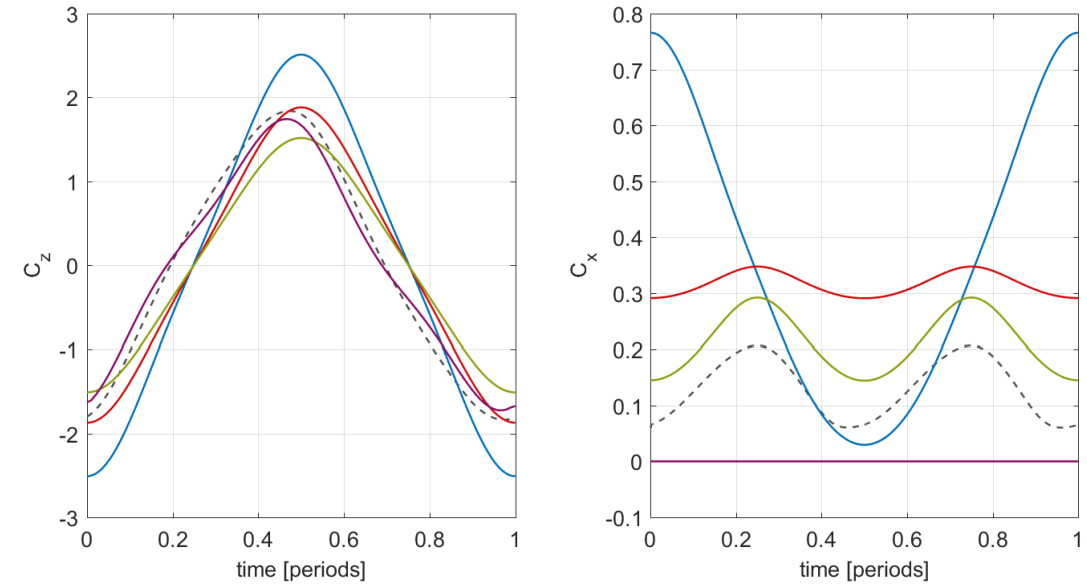


**Figure** 31: Forward flight, $AR = 2$, $R = 0.5$. (- - -) DNS result, (—) Dickinson et al., (—) Wang et al., (—) Dickson and Dickinson, (—) Moriche.

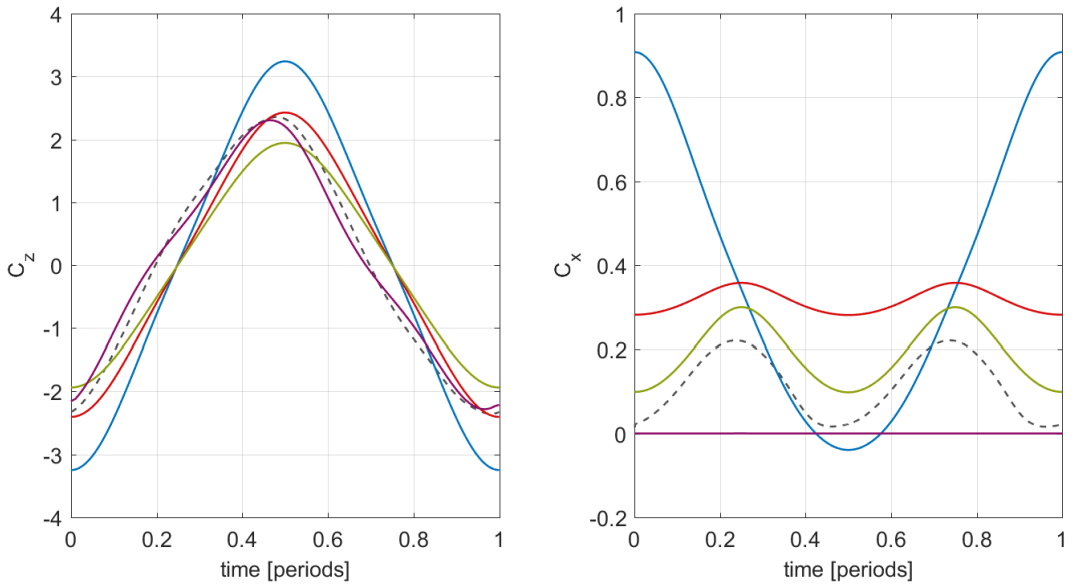


**Figure** 32: Forward flight, $AR = 2$, $R = 2$. (- - -) DNS result, (—) Dickinson et al., (—) Wang et al., (—) Dickson and Dickinson, (—) Moriche.

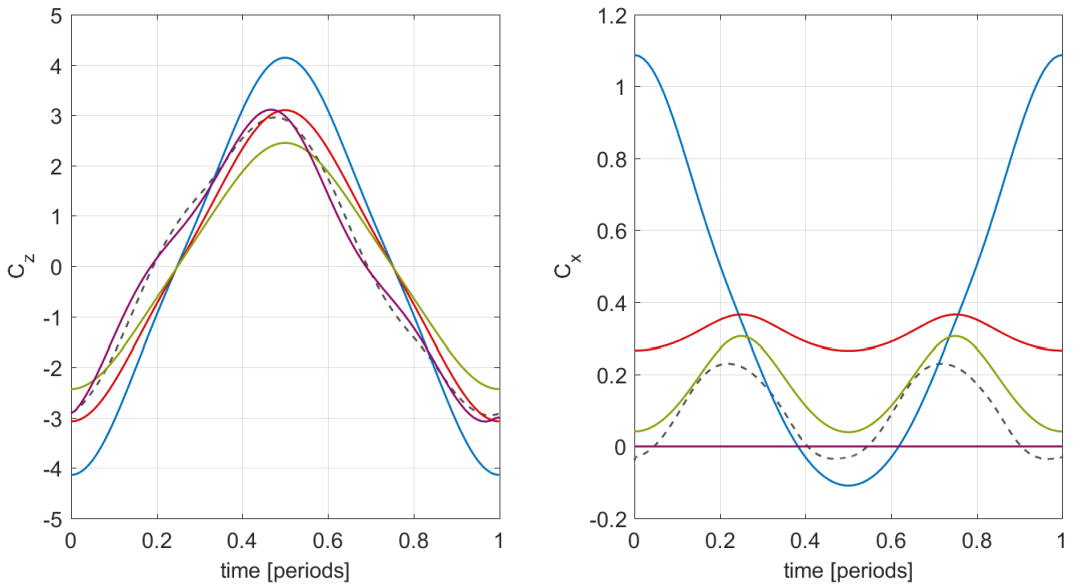


**Figure** 33: Forward flight, $AR = 2$, $R = 8$. (- - -) DNS result, (—) Dickinson et al., (—) Wang et al., (—) Dickson and Dickinson, (—) Moriche.

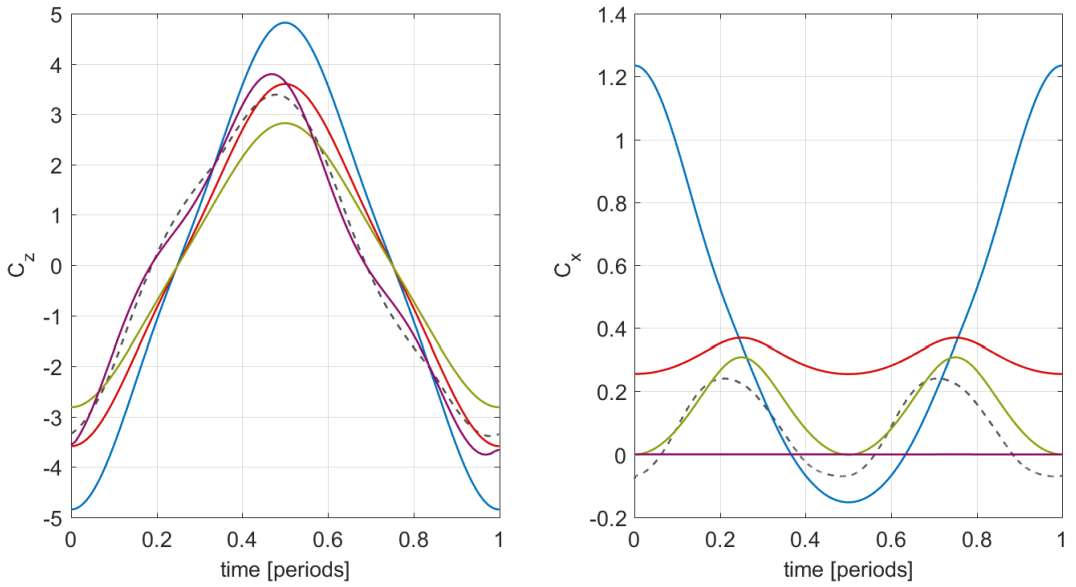


**Figure** 34: Forward flight, $AR = 2$, $R = \infty$. (- - -) DNS result, (—) Dickinson et al., (—) Wang et al., (—) Dickson and Dickinson, (—) Moriche.

## AR = 4

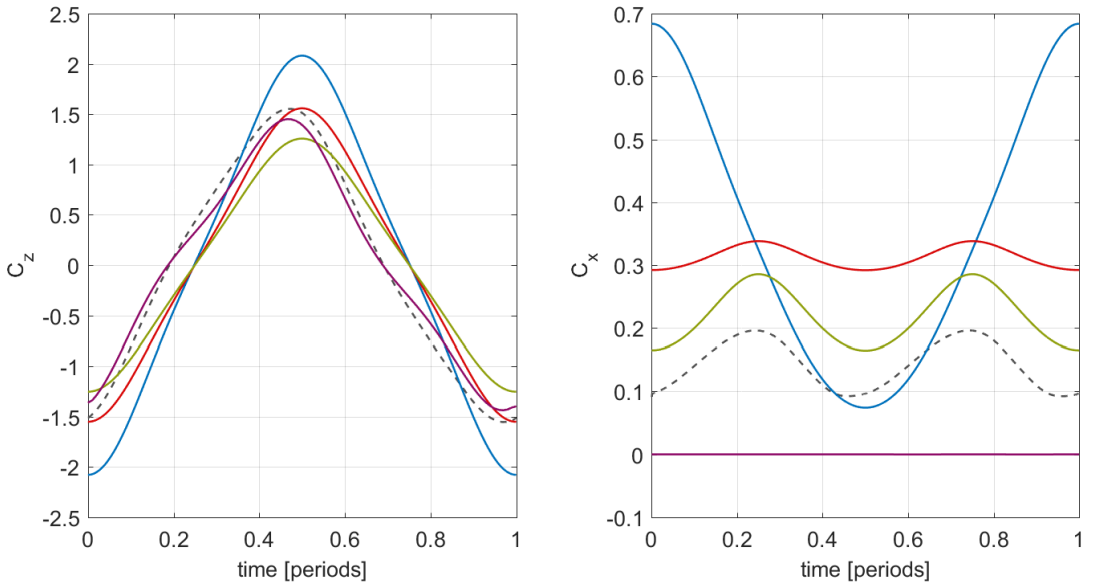


**Figure** 35: Forward flight, $AR = 2$, $R = 0$. (- - -) DNS result, (—) Dickinson et al., (—) Wang et al., (—) Dickson and Dickinson, (—) Moriche.

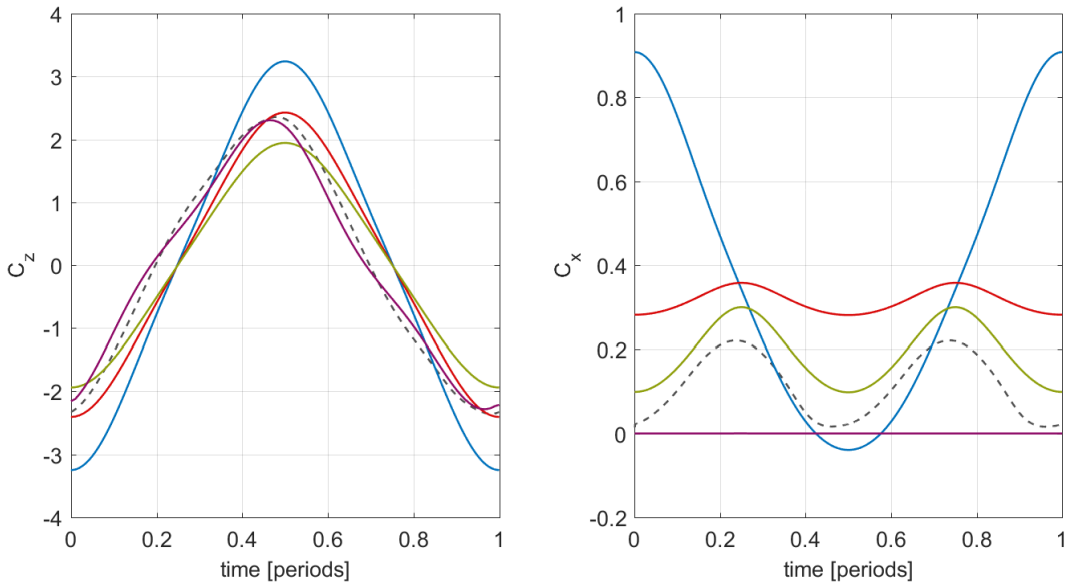


**Figure** 36: Forward flight, $AR = 2$, $R = 2$. (- - -) DNS result, (—) Dickinson et al., (—) Wang et al., (—) Dickson and Dickinson, (—) Moriche.

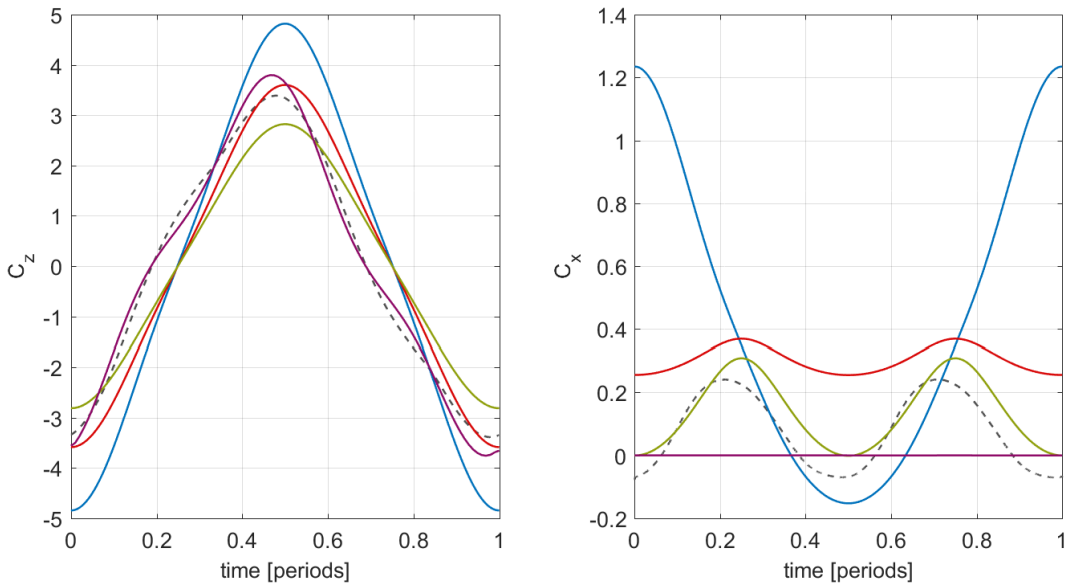


**Figure** 37: Forward flight, $AR = 2$, $R = \infty$. (- - -) DNS result, (—) Dickinson et al., (—) Wang et al., (—) Dickson and Dickinson, (—) Moriche.

# D Results for Hover

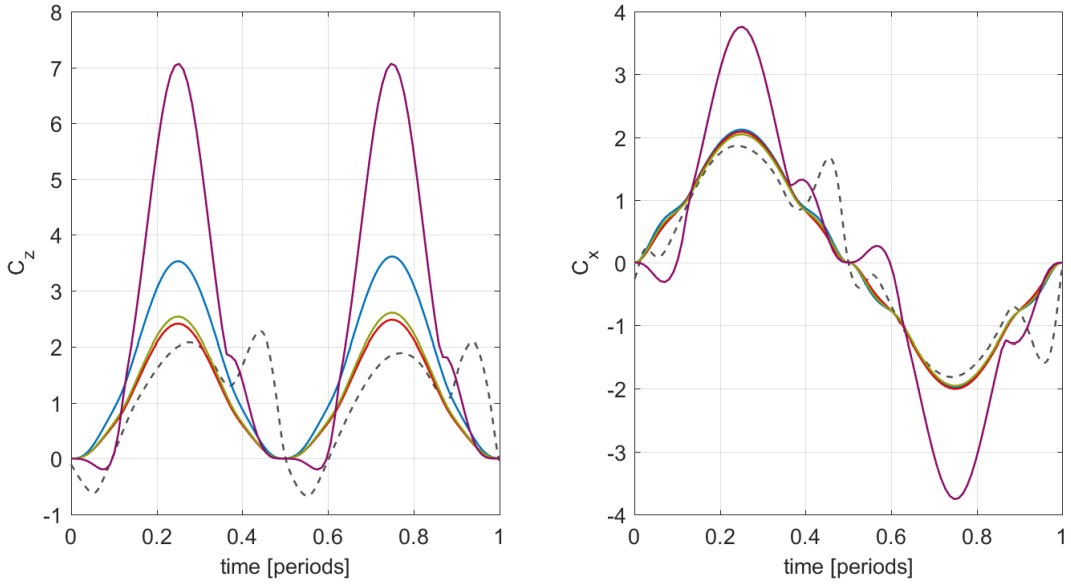


**Figure** 38: Hover, bumblebee (*Bombus hortorum*). (- - -) DNS result, (—) Dickinson et al., (—) Wang et al., (—) Dickson and Dickinson, (—) Moriche.

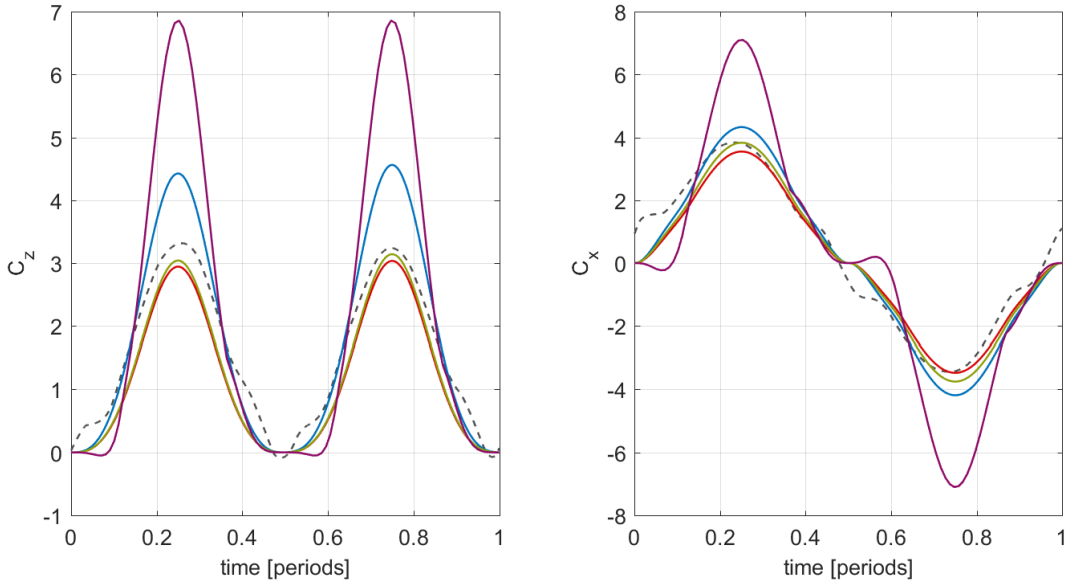


**Figure** 39: Hover, fruit fly (*Drosophilia melanogaster*). (- - -) DNS result, (—) Dickinson et al., (—) Wang et al., (—) Dickson and Dickinson, (—) Moriche.

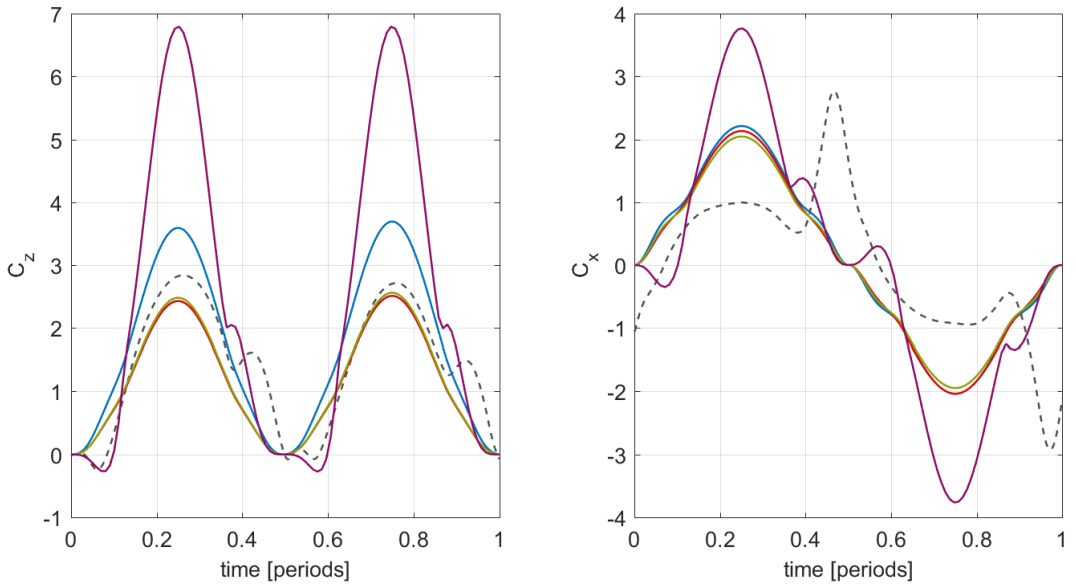


**Figure** 40: Hover, hoverfly (*Episyrphas balteatus*). (- - -) DNS result, (—) Dickinson et al., (—) Wang et al., (—) Dickson and Dickinson, (—) Moriche.

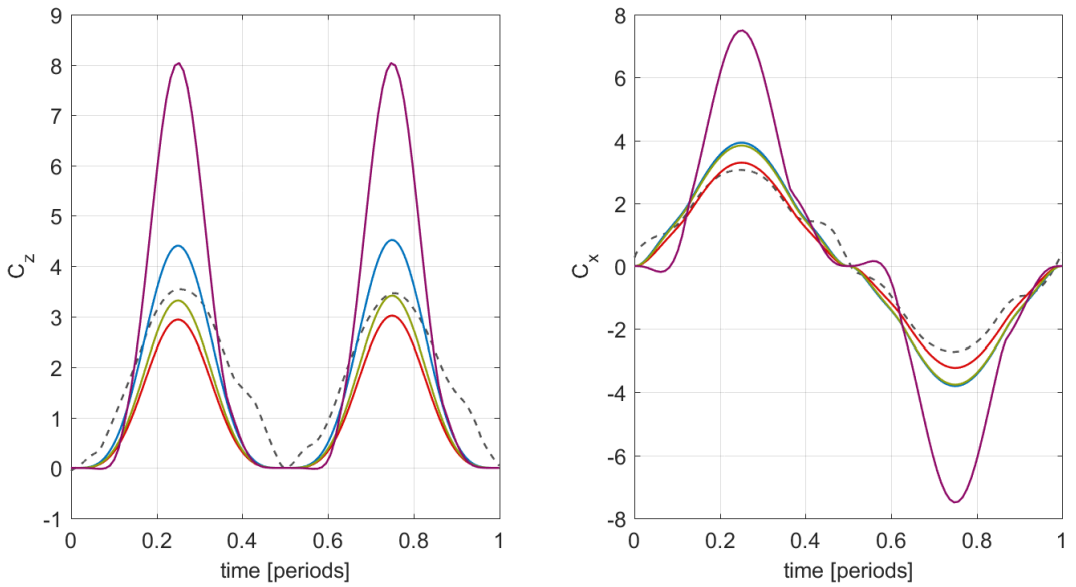


**Figure** 41: Hover, ladybug (*Coccinellidae septempunctata*). (- - -) DNS result, (—) Dickinson et al., (—) Wang et al., (—) Dickson and Dickinson, (—) Moriche.

# References


[1] F. M. Bos, B. W. van Oudheusden, and H. Bijl. Wing performance and 3D vortical structure formation in flapping flight. *Journal of Fluids and Structures*, 2013.

[2] C. C. Chang. Potential flow and forces for incompressible viscous flow. *Mathematical and Physical Sciences*, 437(1901):517–525, 1992.

[3] M. H. Dickinson, F. O. Lehmann, and S. P. Sane. Wing rotation and the aerodynamic basis of insect flight. *Science*, 284:1953–1960, 1999.

[4] W. B. Dickson and M. H. Dickinson. The effect of advance ratio on the aerodynamics of revolving wings. *Experimental Biology*, 207:4269–4281, 08 2004.

[5] C. P. Ellington. The aerodynamics of hovering insect flight. II. morphological parameters. *Philosophical Transactions of the Royal Society of London*, 305:17–40, 1984.

[6] C. P. Ellington, C. V. den Berg, A. P. Willmott, and A. L. R. Thomas. Leading-edge vortices in insect flight. *Nature*, 384:626–630, 1996.

[7] European Aviation Safety Agency. Notice of proposed amendment. Introduction of a regulatory framework for the operation of drones, 05 2017.

[8] T. E. Fritz and N. L. Long. Object-oriented unsteady vortex lattice method for flapping flight. *Journal of Aircraft Engineering and Aerospace Technology*, 41(6):464–474, 2004.

[9] M. Ghommem, M. R. Hajj, D. T. Mook, B. K. Stanford, P. S. Beran, R. D. Snyder, and L. T. Watson. Global optimization of actively morphing flapping wings. *Journal of Fluids and Structures*, 2012.

[10] A. Gonzalo Grande, O. Flores Arias, and M. García-Villalba. A numerical study of finite aspect ratio wings in flapping motion at low Reynold numbers. In *Proceedings of European Fluid Mechanics Conference 11*, 2016.

[11] Y. J. Lee, K. B. Lua, and T. T. Lim. Aspect ratio effects on revolving wings with Rossby number consideration. *Bioinspiration & Biometrics*, 11(5), 2016.

[12] A. Martín Alcántara, R. Fernández Feria, and E. Sanmiguel Rojas. Vortex flow structures and interactions for the optimum thrust efficiencyt of a heaving airfoil at different mean angles of attack. *Physics of Fluids*, 27, 2015.

[13] E. Morales Tirado. Aerodynamic models for high-amplitude, low reynolds flapping airfoils. Bachelor thesis, Universidad Carlos III de Madrid, 09 2015.

[14] M. Moriche Guerrero. *A numerical study on the aerodynamic forces and the wake stability of flapping flight at low Reynolds number*. PhD thesis, Universidad Carlos III de Madrid, 2017.

[15] U. Pesavento and Z. J. Wang. Falling paper: Navier-stokes solutions, model of fluid forces, and center of mass elevation. *Physical Review Letters*, 93(14), 2004.

[16] E. C. Polhamus. A concept of the vortex lift of sharp-edge delta wing based on a leading edge suction analogy. *NASA Techinical Report*, 1966.

[17] R. Ramamurti and W. Sandberg. A three-dimensional computational study of the aerodynamic mechanisms of insect flight. *Journal of Experimental Biology*, 205(10):1507–1518, 2002.

[18] J. M. Seddon and S. Newman. *Basic helicopter aerodynamics*. Wiley & Sons, 2011.

[19] S. Shkarayev and D. Silin. Application of actuator disk theory to membrane flapping wings. *AIAA Journal*, 48(10):2227–2234, 10 2010.

[20] W. Shyy, H. Aono, C.-K. Kang, and H. Liu. *An Introduction to Flapping Wing Aerodynamics*. Cambridge University Press, 2013.

[21] M. Stolpe and K. Zimmer. Der Vogelflug. Seine anatomisch-physiologischen und physikalisch-aerodynamischen Grundlagen. *Akademische Verlagsgesellschaft*, 1939.

[22] M. Sun and G. Du. Lift and power requirements of hovering insect flight. *Acta Mechanica sinica*, 19(5):456–469, 10 2003.

[23] M. Sun and J. Tang. Lift and power requirements of hovering flight in drosophilia virilis. *Journal of Experimental Biology*, 205:2413–2427, 2002.

[24] H. E. Taha, M. R. Hajj, and A. H. Nayfeh. Flight dynamics and control of flapping-wing MAVs: a review. *Springer*, 70:907–939, 07 2012.

[25] K. Taira and T. Colonius. Three-dimensional flows around low-aspect-ratio flat-plate wings at low Reynolds numbers. *Journal of Fluid Mechanics*, 623:187–207, 2009.

[26] Z. J. Wang, J. M. Birch, and M. H. Dickinson. Unsteady forces and flows in low reynolds number hovering flight: two-dimensional computations vs robotic wing experiments. *Journal of Experimental Biology*, 207:449–460, 10 2003.

[27] T. Weis-Fogh. Energetics of hovering flight in hummingbirds and drosophilia. *Journal of Experimental Biology*, 56:79–104, 1972.

[28] T. Weis-Fogh and M. Jensen. Biology and physics of locust flight. basic principles of insect flight. a critical review. *Philosophical Transactions of the Royal Society of Biological Sciences*, 239:415–458, 1956.